



UNIVERSITY OF ZURICH
DEPARTMENT OF PHYSICS

Characterization of silicon photomultiplier arrays in liquid xenon and development of dedicated read-out electronics

MASTER THESIS IN PHYSICS

author:

Sandro D'AMATO

supervised by

Prof. Dr. Laura BAUDIS

Dr. Alexander KISH

M.Sc. Julien WULF

JULY 14, 2016

Summary

The future experiment DARWIN (DARK matter WImp search with liquid xenoN) will employ a multi-ton, xenon-based Time Projection Chamber (TPC) to search for dark matter. The primary goal of DARWIN will be to explore all experimentally accessible parameter space for Weakly Interacting Massive Particles (WIMPs), which will ultimately be limited by irreducible neutrino backgrounds.

The prompt scintillation light and the charge signals induced by particle interactions in the xenon target inside the TPC, will be observed by sensitive, ultra-low background photosensors. For that purpose a future version of the photomultiplier tubes (PMTs) employed in the XENON1T dark matter search experiment could be used. Although PMTs are reliable and proven to work in noble liquid TPCs, they are expensive, bulky and generate a significant fraction of the radioactive background in dark matter detectors. This is the reason why alternative light read-out techniques are under consideration by the collaboration. A promising candidate is the silicon photomultiplier (SiPM): its technology is rapidly developing and may become suitable for the read-out of large detectors, offering very low radioactivity levels, compact geometry and low operation voltages.

In the scope of this thesis the 10943-3186(x) Type A Hamamatsu SiPM prototype was extensively characterized in gaseous and liquid xenon, using a temperature controlled cryostat. A detailed feedback was given to the manufacturer about the performance parameters and noise components. Furthermore as an R&D step for DARWIN, different types of read-out boards have been designed for the operation of the considered SiPM.

This work is structured as follows: Chapter 1 gives a brief introduction about dark matter and the direct detection principles of a dual-phase xenon TPC. The future dark matter experiment DARWIN is shortly introduced, giving the motivation for the possible use of SiPMs as photosensors. In the first half of Chapter 2 the physical working principle of generic photodiodes is explained and the working principle and operation of the single-pixel avalanche photodiode (APD) and the multi-pixel SiPM is elaborated. The second half of Chapter 2 is dedicated to the performance parameters of a SiPM and various experimental methods to evaluate them. Chapter 3 introduces first the investigated SiPM prototype and then presents different principles of dedicated read-out electronics. The focus is set on the design of three prototype read-out boards, including the integration of a pre-amplifier circuit. The results of the measured performance parameters are presented in Chapter 4, introducing a novel method to evaluate the after-pulse probability. The conclusions and an outlook for future R&D are given in Chapter 5.

Acknowledgements

I owe my deepest gratitude to Dr. Prof. Laura Baudis for giving me the great opportunity to contribute to the R&D process of a cutting edge future experiment like DARWIN and being a member of the XENON Collaboration. I want to thank Dr. Alexander Kish for his great support in the laboratory and his help during every step of my thesis.

This thesis would not have been possible without Julien Wulf. His encouragement, support, and invaluable suggestions made this work successful. He has been everything that one could want in an advisor and a friend.

I am deeply indebted to Camilla Galloni and Deborah Pinna for their time and effort in reviewing this work.

My sincere thanks go to Roman Gredig for his help during my first steps with SiPMs and to Daniel Florin for his suggestions regarding the read-out electronics.

A special thank goes to all my friends and especially to Gaudenz Kessler and Chris Marantini for the endless ours of company in the library during my time at the university.

Finally, I wish to thank my dearest ones, my girlfriend Camilla, my parents Giuseppe and Adriana and my brother Maurizio for their love, support, patience and encouragement during all my academic studies.

Contents

1	Introduction	1
1.1	Dark matter in the Universe	1
1.2	Noble liquid dark matter detectors	1
1.3	DARWIN the ultimate dark matter detector	2
1.4	Silicon photomultipliers as replacement for PMTs	5
2	Silicon photomultiplier (SiPM)	6
2.1	The physics of a silicon photodiode	6
2.1.1	The p-n junction	6
2.1.2	Avalanche photodiode (APD)	7
2.2	Operation of APDs and SiPMs	8
2.2.1	Avalanche photodiode in Geiger mode	10
2.2.2	SiPM operation	11
2.3	Performance parameters of a SiPM	12
2.3.1	Experimental evaluation of operational parameters	12
2.3.2	Noise components of a SiPM	14
3	Read-out electronics and tested SiPM prototype	18
3.1	Single-channel read-out electronics	20
3.2	Multi-channel read-out electronics	21
3.3	Pre-amplifier read-out electronics	22
4	Measurements and Results	26
4.1	Forward-bias I-V characteristics	26
4.2	Gain calibration	27
4.3	Dark count rate	30
4.4	Cross-talk probability	32
4.5	After-pulse probability	32
4.6	Scintillation light detection in LXe	36
5	Conclusions and outlook	38
5.1	Performance parameters	38
5.2	Read-out electronics	39
5.3	Future R&D plans	39

List of Figures

1.1	Upper limits of present and future experiments of the WIMP-nucleon scattering parameter space for spin-independent interaction.	3
1.2	Particle detection principle of a dual-phase xenon TPC.	4
2.1	Band-gap diagram for zero bias (top), forward bias (middle) and reverse bias (bottom) of a silicon p-n junction.	8
2.2	Different doped layers of a reverse biased APD showing the corresponding electric field strength.	9
2.3	Equivalent circuit of a SiPM.	9
2.4	Equivalent circuit of an APD in Geiger mode in series with a resistor R_Q	10
2.5	Current flowing through the terminals of the APD as a function of time.	11
2.6	Equivalent circuit of a SiPM.	12
2.7	(left) Forward and reverse I-V characteristics of a SiPM. (right) The electrical circuit to obtain a forward-bias I-V characteristic.	13
2.8	(left) Experimental setup to measure the gain and the breakdown voltage. (middle) Sketch of a charge photoelectron (p.e.) spectrum. (right) Sketch of the gain versus bias voltage of a SiPM.	14
2.9	Oscilloscope screen shot with visible noise components.	15
2.10	(left) Experimental setup to measure the dark count rate (DCR) and the cross-talk rate (CTR). (right) Sketch of the threshold-dependent dark count rate.	16
3.1	Technical drawing of SiPM 10943-3186(x) Type A.	19
3.2	(left) Schematic of the single read-out circuit. (right) PCB routing.	20
3.3	Signal pulse shape of a SiPM for serial, single and parallel read-out.	21
3.4	(left) Schematic of the hybrid read-out circuit. (right) PCB board routing of the hybrid read-out.	22
3.5	(left) Waveform acquired with the hybrid read-out board. (right) Photoelectron spectrum acquired with a hybrid read-out board, without resolved p.e. peaks.	23
3.6	Schematic of single read-out pre-amplifier circuit with a gain of 20. The central piece is a non-inverting voltage feedback operational amplifier.	23
3.7	(left) Schematic of a non-inverting voltage feedback operational amplifier. (right) Illustration of the corresponding potential divider network.	24
3.8	(left) Pre-amplifier performance test setup at room temperature. (right) Photoelectron spectrum of the SiPM.	25

4.1	(left) Forward-bias voltage I-V characteristics of all segments at 23.5°C temperature. (right) The same at -99.5°C temperature.	26
4.2	(left) Experimental setup for the gain measurements. (right) Picture of the SiPM on a single read-out board fixed on a PTFE (Teflon) holding structure.	27
4.3	(left) Example of a waveform with one single (p.e.) event. (right) Example of a photoelectron spectrum with the dominant noise peak around zero and the following p.e. peaks.	28
4.4	(left) Gain calibration curve in GXe at 23.5°C. (right) Gain calibration curve in LXe at -99.5°C.	29
4.5	(left) The 1 p.e. peak resolution as a function of the overvoltage at 23.5°C. (right) The 1 p.e. peak resolution as a function of the overvoltage at -99.5°C.	30
4.6	Experimental setup for the DCR measurements as a function of the overvoltage and threshold.	31
4.7	(left) Measurement of the threshold depended DCR of segment 1 in warm. (right) Pulse amplitude p.e. spectrum.	31
4.8	(left) Overvoltage-dependent DC rate at room temperature (23.5°C). (right) Overvoltage-dependent DC rate at LXe temperature (-99.5°C).	32
4.9	(left) Overvoltage-dependent CT probability at room temperature (23.5°C). (right) Overvoltage-dependent CT probability at LXe temperature (-99.5°C).	33
4.10	A waveform with an after-pulse event. Note the after-pulse peak a few ns after the primary peak.	33
4.11	Pulse-charge versus Pulse-height representation of the 1 p.e. peak of segment 1 at -99.5°C.	34
4.12	(left) The after-pulse probability as a function of the overvoltage at 23.5°C. (right) The after-pulse probability as a function of the overvoltage at -99.5°C.	35
4.13	Experimental setup for the xenon scintillation light measurement.	36
4.14	Energy spectrum of the employed ^{241}Am α -particle source.	37
4.15	Acquired α -particle spectrum of the 10943-3186(x) Type A SiPM.	37

1 Introduction

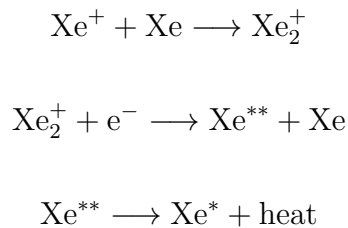
1.1 Dark matter in the Universe

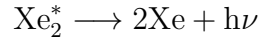
Consistent evidence from a range of astronomical and cosmological observations indicates that a significant part of the content of the Universe is composed of cold dark matter [1–4]. Detailed studies of the cosmic microwave background anisotropies have determined the abundance of dark matter with noticeable precision at $(26.0 \pm 0.5)\%$ [5, 6]. Weakly Interacting Massive Particles (WIMPs) is a generic class of dark matter candidates, arising naturally in many theories beyond the Standard Model of particle physics, such as supersymmetry, little Higgs models, or extra-dimensions [7–9].

1.2 Noble liquid dark matter detectors

Noble liquid detectors aim to measure the scintillation signal and the ionisation signal of a nucleon-WIMP scattering. Xenon can be used as target material, since the noble gas has many advantages for particle detection. It is an efficient and fast scintillator. The high density of liquid xenon (LXe) of about 3 g/cm^3 provides a good self-shielding and a compact detector geometry. The absence of long-lived radioactive isotopes, apart from ^{136}Xe , ensures that an ultra-low background level can be achieved.

When a WIMP interacts with a xenon atom, the energy transfer is split between ionization, excitation and heat. The 178 nm wavelength scintillation light is produced in two different ways, shown in equation 1.1 and 1.2, involving excited atoms (Xe^*) and ions (Xe^+), both produced by ionizing radiation [10].





(1.2)

In both processes, one exciton or ion produces one ultraviolet photon, $h\nu$ following the creation and radiative decay of an excited dimer, Xe_2^* . The lifetimes for the singlet and triplet states of the excited dimer have been measured to be about 2 ns and 30 ns in liquid xenon [11].

Detectors using LXe as target material to directly detect WIMP interactions have demonstrated the highest sensitivities over the past years for a WIMP mass higher than $6 \text{ GeV}/c^2$ [12]. The XENON100 experiment published in 2012 and 2013 the world's best upper limits on the spin-independent [13] and spin-dependent [14] coupling of WIMPs to nucleons and neutrons, respectively. Those results were confirmed and improved by the LUX experiment [15], also using LXe as target material.

To probe lower cross sections at WIMP masses above a few GeV/c^2 , larger detectors are required: The current phase in the XENON program at the Laboratori Nazionali del Gran Sasso (LNGS), called XENON1T, has a 2 ton LXe target and aims to reach spin-independent cross sections of $1.6 \times 10^{-47} \text{ cm}^2$ after 2 years of continuous operation [16]. The upgrade phase XENONnT is being designed and will be constructed during the operation of XENON1T with an increased sensitivity of another order of magnitude [16]. The same sensitivity is projected for the next phase of the LUX program [17] called LUX-ZEPLIN (LZ). The DarkSide collaboration proposes a 20 ton liquid argon dual-phase detector, with a goal to reach $9 \times 10^{-48} \text{ cm}^2$ at $1 \text{ TeV}/c^2$ [18, 19].

1.3 DARWIN the ultimate dark matter detector

DARk matter WImp search with liquid xenoN (DARWIN) will be a multi-ton, xenon-based dual-phase time projection chamber (TPC) to directly detect dark matter with a sensitivity beyond all the above mentioned projects. The primary goal of DARWIN will be to explore all experimentally accessible parameter space for WIMPs, which will ultimately be limited by irreducible neutrino backgrounds from neutrino-nucleus scattering in the target material. A 40 ton active LXe target will allow probing WIMP masses in the range $5 \text{ GeV}/c^2 - 100 \text{ TeV}/c^2$, and WIMP-nucleon cross sections down to the few $\times 10^{-49} \text{ cm}^2$ region for $\sim 50 \text{ GeV}/c^2$ WIMPs [20]. In figure 1.1 the current and expected sensitivities to spin-independent WIMP-nucleon interactions are summarized as a function of the WIMP mass for noble liquid detectors [13, 16–18, 21–25].

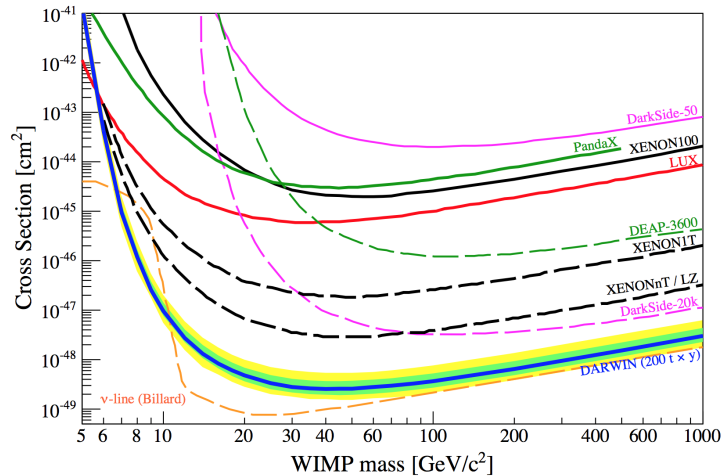


Figure 1.1: The results and expectations of various noble liquid detectors are represented. Along with the existing upper limits from PandaX- II [21], DarkSide-50 [22], XENON100 [13], and LUX [23], are the sensitivity projections for DEAP3600 [24], XENON1T [16], XENONnT [16], LZ [17], DarkSide-20k [18] and DARWIN [25]. DARWIN is designed to probe the entire parameter region for WIMP masses above $\sim 5\text{GeV}/c^2$, until the neutrino background (ν -line) will start to dominate the recoil spectrum. Figure from [26].

Figure 1.2 shows the sketch of a dual-phase xenon TPC. The nucleon-WIMP scattering produces a prompt scintillation light (S1) and gets detected by photosensors on the top and bottom of the target volume. With an applied electric field E_d across the liquid xenon target, some of the ionization electrons are removed from the interaction site, do not recombine and can be detected independently from the S1 light signal. These electrons are drifted and extracted into the gas phase above the liquid xenon target, and accelerated with a high electric field E_g , producing an electro-luminescence signal (S2) via collisions with xenon atoms, which is detected by the photosensor arrays above and below the target volume. Mapping the photosensor response from the S2 signal gives the xy-position of the interaction vertex, while the time difference between the S1 and S2 signals provides information about on the z-coordinate of the interaction.

The photosensors for DARWIN could be a future version of the XENON1T photo-multiplier tubes (PMTs). These sensors feature a high quantum efficiency at 178 nm, a very low intrinsic radioactivity, a high photo-cathode uniformity, a high gain and a low dark count rate [27–29]. Although PMTs are reliable and proven to work in noble liquid TPCs, they are expensive, bulky and still generate a significant fraction of the radioactive background in dark matter detectors, especially in terms of radiogenic nuclear recoils [20]. This is the reason why alternative light read-out techniques are under consideration for the future experiment.

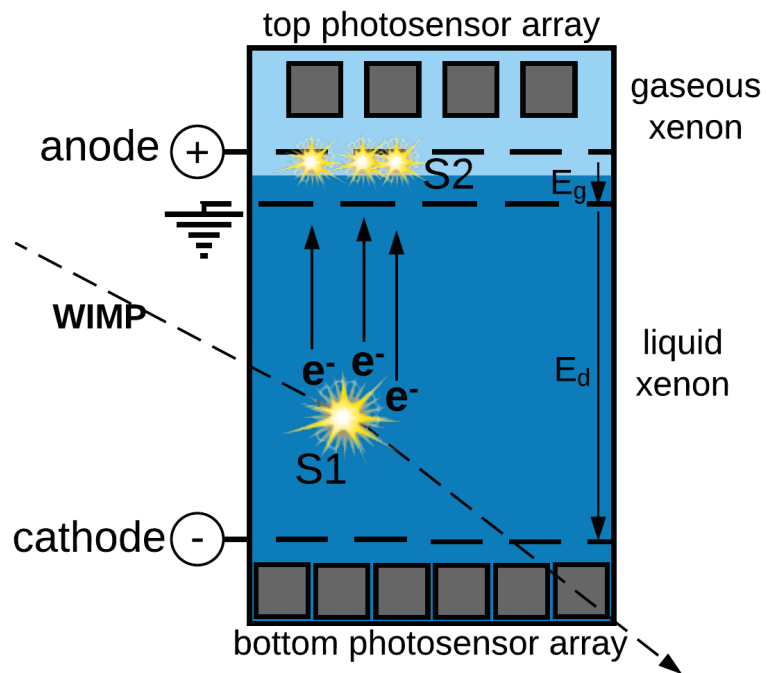


Figure 1.2: Particle detection principle of a dual-phase xenon TPC. The WIMP scatters at the xenon atom and creates a prompt scintillation light (S1). The ionization electrons are removed from the interaction side with a drift field E_d , extracted into the gas phase with an electric field E_g and there detected as scintillation light (S2).



1.4 Silicon photomultipliers as replacement for PMTs

A promising replacement candidate is the silicon photomultiplier (SiPM), since its technology is rapidly developing and may become suitable for the read-out of large detectors, offering very low radioactivity levels, compact geometry and low operation voltages. They would allow an increase of the photosensitive area coverage of the TPC, and in principle might be suitable for a 4π coverage. Commercially available SiPMs operate well at LXe temperatures [30] and are comparable to state-of-the-art PMTs, having photo-detection-efficiency (PDE) values of $\sim 10\text{-}25\%$ at 178 nm [31] and gains of a few $\times 10^6$. However, the use of SiPM arrays for photon detection in large-volume dark matter LXe detectors still requires significant improvements. Especially, the currently best dark count rate (DCR) of $\sim 1\text{Hz}/\text{mm}^2$ at LXe temperatures [31], should be reduced by at least 2 orders of magnitude in order to keep accidental coincidence low enough for the desired detection thresholds. The correlated noise probabilities of a SiPM, namely the after-pulse (AP) and cross-talk (CT) probability, requires further studies and improvements. Using an SiPM as a light detector in scientific research requires that its optical and electrical behaviour under varied environmental conditions, the types and rates of noise, and the limits on reliable light detection are well understood. Although manufacturers of SiPMs provide information on their products, an independent check of the detector characteristics is necessary, especially in critical situations where a scientific breakthrough hinges on the validity of the observations.

In the scope of this thesis the Hamamatsu SiPM prototype 10943-3186(x) Type A was extensively characterized in gaseous and liquid xenon, giving a detailed feedback to the manufacturer. Furthermore as an R&D step for DARWIN, different types of read-out boards that can be operated directly in the LXe have been designed and tested.

2 Silicon photomultiplier (SiPM)

This chapter gives an introduction to the physical and electronic working principles of a silicon photomultiplier (SiPM) and describes in detail the experimental techniques to characterize the most important properties of a SiPM. The physical processes that take place inside a generic photodiode are explained in Section 2.1. The basic principles behind the operation of first a simple avalanche photo diode (APD) and then a multi-pixel SiPM are described in Section 2.2. The most relevant performance parameters of a SiPM are presented in Section 2.3 along with the experimental methods to quantify them.

2.1 The physics of a silicon photodiode

2.1.1 The p-n junction

A boundary between two types of semiconductor material, p-type and n-type, inside a single crystal of semiconductor is called p-n junction. The "p" (positive) side contains an excess of electron holes, while the "n" (negative) side contains an excess of electrons. The excess of charge carriers in p-n junctions is created by doping the material, for example by ion implantation [32]. Silicon atoms have 4 valence electrons. In a silicon crystal those electrons form covalent bonds with the electrons from neighbouring Si-atoms, making the crystal an insulator. If for example a phosphorus atom, which has 5 valence electrons, is implanted into the Si-lattice, a free electron is introduced. This makes the P-atom an electron donor. If on the other hand an aluminium atom is implanted (with 3 valence electrons), a free electron hole is introduced into the lattice, hence the Al-atom is an electron acceptor. The notations for the different doping concentrations are given in table 2.1.

symbol	dopant concentration
i	intrinsic Si (zero dopant)
p	1 acceptor/ 10^6 Si-atoms
n	1 donor/ 10^7 Si-atoms
p ⁺	1 acceptor/ 10^4 Si-atoms
n ⁺	1 donor/ 10^4 Si-atoms

Table 2.1: Dopant concentrations of silicon crystals with the respective symbolic notations.

The p–n junction possesses some interesting properties that have useful applications in modern electronics. A p-doped and an n-doped semiconductor is relatively conductive, but the junction between them can become depleted of charge carriers, and hence non-conductive. This property depends on the relative voltages of the two semiconductor regions. The application of a voltage across a p–n junction is called "bias". The simplest electronic component containing a p-n junction is a diode, allowing current to flow only in one direction, depending on the bias.

zero bias For a p-n junction at zero bias (see figure 2.1), the Fermi levels E_F [32] match on the two sides of the junctions. Electrons and holes reach an equilibrium at the junction and form a depletion region. The upward direction in figure 2.1 represents increasing electron energy. That implies that you would have to supply energy to get an electron to go up or to get a hole to go down in the diagram.

forward bias To forward-bias the p-n junction, the p side is made more positive, so that it is "downhill" for electron motion across the junction. The depletion region becomes smaller and an electron can move across the junction and fill a vacancy or "hole" near the junction. It can then move from vacancy to vacancy leftward (see figure 2.1) toward the positive terminal, which could be described as the hole moving right. The conduction direction for electrons in figure 2.1 is right to left.

reverse bias To reverse-bias the p-n junction, the p side is made more negative, making it "uphill" for electrons moving across the junction. The depletion zone becomes bigger, making the p-n junction non-conductive (see figure 2.1 bottom).

2.1.2 Avalanche photodiode (APD)

The difference between an APD and an ordinary p-n junction photodiode is that an APD is designed to support high electric fields. An electron-hole pair is generated by the absorption of a photon with sufficient energy in the non-doped (intrinsic) region "i" (see figure 2.2). The minimal photon energy is 1.1 eV in the case of silicon (Si) [32]. Such charge carrier pairs can also be thermally generated, resulting in leakage current, which is also called dark current because it is present even in the absence of incident light. Under the influence of the field, the electron drifts to the n^+ side and the hole drifts to the p^+ side, resulting in the flow of a photocurrent. The drift velocity for high electric fields in Si, is about 10^7 cm/sec [33] for both electrons and holes. The charge carriers can gain sufficient energy in the high field at the p- n^+ junction to collide with the crystal lattice and generate another electron-hole pair, losing some of their kinetic energy in the process. This process is known as impact ionization. The charge carriers can accelerate again, as the secondary electron or hole, and create more electron-hole pairs. After a few transit times, a competition develops between the rate at which electron-hole pairs are being generated by impact ionization and the rate at which they exit the high-field region and are collected. If the magnitude of the reverse-bias voltage is below a value

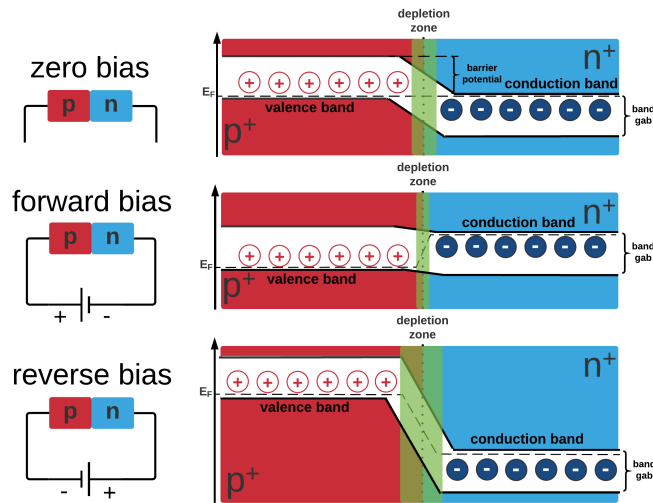


Figure 2.1: Band-gap diagram for zero bias (top), forward bias (middle) and reverse bias (bottom) of a silicon p-n junction. The depletion zone decreases for forward bias making the junction conductive and increases for reverse bias making the junction non conductive.

known as the breakdown voltage, the collection dominates, causing the population of electrons and holes to decline.

Figure 2.2 illustrates the process of electron-hole generation, drift, and collection for an APD. The electron trajectories are represented by black arrows, and the hole trajectories by red arrows. When a photodiode is used to detect light, the number of electron-hole pairs generated per incident photon, a value defined as quantum efficiency (QE) is at best unity. Losses due to reflection or absorption in regions with low or zero electric field lower the QE.

2.2 Operation of APDs and SiPMs

Silicon photomultipliers (SiPMs) consists of several pixels connected in parallel; one pixel is a combination of an APD and a quenching resistor R_Q connected in series, as illustrated in figure 2.3.

It is operated with an external reverse-biased voltage (V_{BIAS}), that is up to a few volts larger than the breakdown voltage (V_{BR}) of the APD. In this mode the electrons and holes multiply by impact ionisation faster than they can be extracted. The overvoltage, $\Delta V = V_{BIAS} - V_{BR}$, is one of the most important adjustable parameters affecting the performance of the detector.

The following two subsections describe in detail, the operation of an APD and a SiPM for $V_{BIAS} > V_{BR}$.

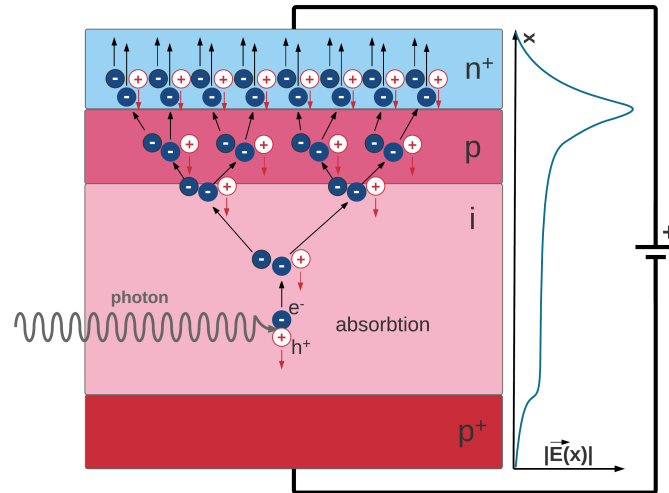


Figure 2.2: Different doped layers of a reverse biased APD showing the corresponding electric field strength. The photon absorption, impact ionisation and avalanche formation are visualized. The electron trajectories are represented by black arrows and the hole trajectories by red arrows.

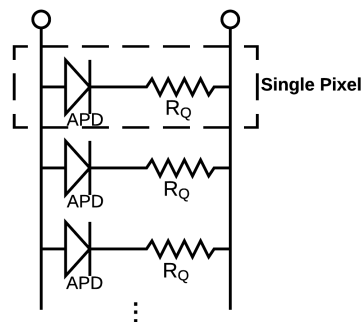


Figure 2.3: Equivalent circuit of a SiPM. A single pixel is a series combination of an avalanche photodiode (APD) and a quenching resistor (R_Q). All the pixels are connected in parallel.

2.2.1 Avalanche photodiode in Geiger mode

When the applied bias voltage V_{BIAS} to an APD exceeds its breakdown voltage V_{BR} , the APD is said to be in Geiger mode [34]. McIntyre (1961) and later Haitz (1964) [35] developed an electrical model for an APD operating in this state. Geiger-mode APDs are modelled by the circuit depicted in figure 2.4, where the main components are: the capacitance C_J of the depletion region of the APD, a switch S , a voltage source V_{BR} , and a series resistance R_S that is equal to the combined resistance of the undepleted regions in the APD. The value of R_S depends on the voltage over the diode since the latter controls the total length of the undepleted regions. R_S is on the order of several hundred ohms at zero bias and decreases to tens of ohms for bias around V_{BR} .

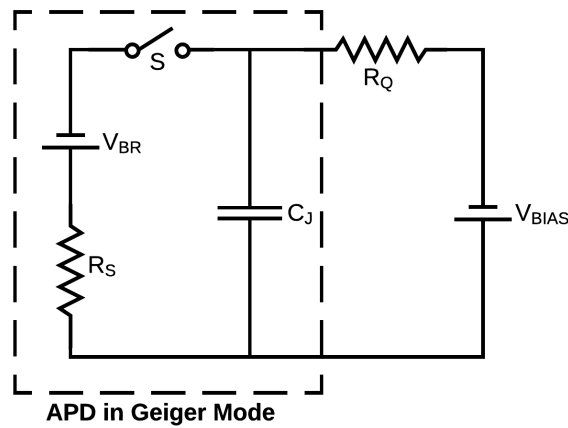


Figure 2.4: Equivalent circuit of an APD in Geiger mode in series with a resistor R_Q . C_J is the capacitance of the depletion region of the APD, the switch S closes when a photon is detected, the voltage source V_{BR} produces the signal pulses, and the series resistance R_S is equal to the combined resistance of the undepleted regions in the APD.

In the absence of light, the switch S is open and C_J is charged to V_{BIAS} . The voltage on the APD is $\Delta V = V_{\text{BIAS}} - V_{\text{BR}}$ above V_{BR} , and the APD is ready to detect a photon. Suppose that the APD absorbs a photon and the resulting charge carrier, either an electron or a hole, triggers an avalanche as seen in figure 2.2. At this instant, the switch S closes and C_J begins to discharge through R_S , which tends to lower the voltage across the APD. However, since the APD is biased by a constant voltage source V_{BIAS} , a current begins to flow through the terminals of the APD reaching a steady state value of $\Delta V/R_S$. This current will persist unless V_{BIAS} is reduced to V_{BR} , restoring the APD to the light-sensitive state. The role of R_Q is to extinguish or quench the avalanche bringing the APD back to Geiger mode, hence the name quenching resistor. The time dependency of the described current flow through the APD is shown in figure 2.5.

The avalanche begins at $t = t_i$. The leading edge of the current pulse increases with the time constant $R_S \times C_J$ and reaches a maximum value of

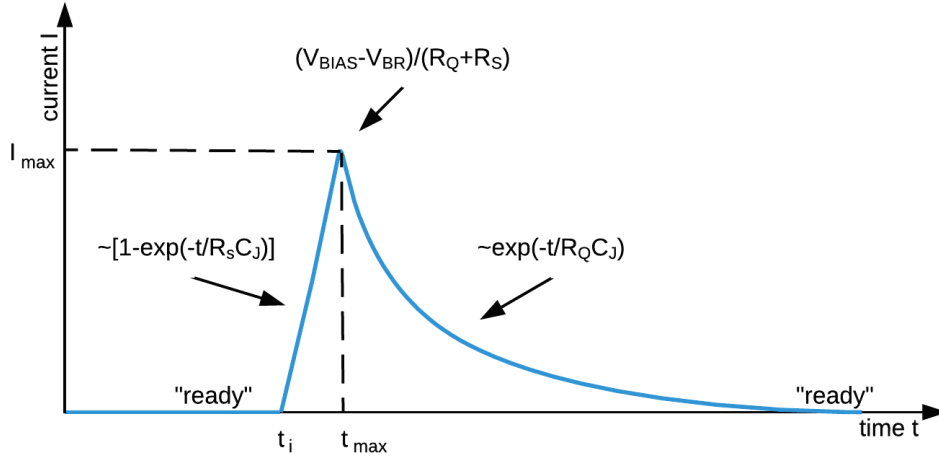


Figure 2.5: Current flowing through the terminals of the APD as a function of time. The pulse is asymmetric around $t = t_{\max}$ because of $R_Q \gg R_S$.

$$I_{\max} = \frac{V_{\text{BIAS}} - V_{\text{BR}}}{R_Q + R_S} \approx \frac{\Delta V}{R_Q} \quad (2.1)$$

at t_{\max} . At around this time the avalanche stops or is quenched because of R_Q . After t_{\max} , C_J recharges to the nominal voltage of V_{BIAS} while the current decreases with a time constant $R_Q \times C_J$. Because $R_Q \gg R_S$, the leading edge of the pulse is steeper than the declining edge, making the pulse asymmetric around $t = t_{\max}$. For a more detailed discussion of the electrical behaviour of Geiger-mode APD see [35].

2.2.2 SiPM operation

A SiPM is an array of light-sensitive elements – pixels – that are all connected in parallel and externally biased by a single voltage source, V_{BIAS} . Each pixel is a series combination of an APD and a quenching resistor R_Q , as described in detail in Section 2.2.1. By design, all pixels are identical. The pixels are operated in Geiger mode ($\Delta V > 0$).

Figure 2.6 shows the equivalent circuit of a SiPM; the dashed rectangle delineates a single pixel. In the absence of light, all the switches are in the OFF position, and the voltage is V_{BIAS} on each APD and is zero on each R_Q . Suppose that a single APD absorbs a photon and the process triggers an avalanche. At this instant, the switch in the equivalent circuit of that APD in figure 2.4 goes to the ON position, and the current pulse begins to flow through the terminals of the SiPM as shown in figure 2.5. The resistor R_Q of that pixel quenches the avalanche, and the pixel is restored back to the "ready" state. If two (or more) photons simultaneously trigger avalanches in two (or more) distinct pixels, the current pulse flowing through the terminals of the SiPM is a superposition of the current pulses. Instead, if a single pixel absorbs simultaneously two or more photons, the resulting current pulse is identical to the one produced by a single photon.

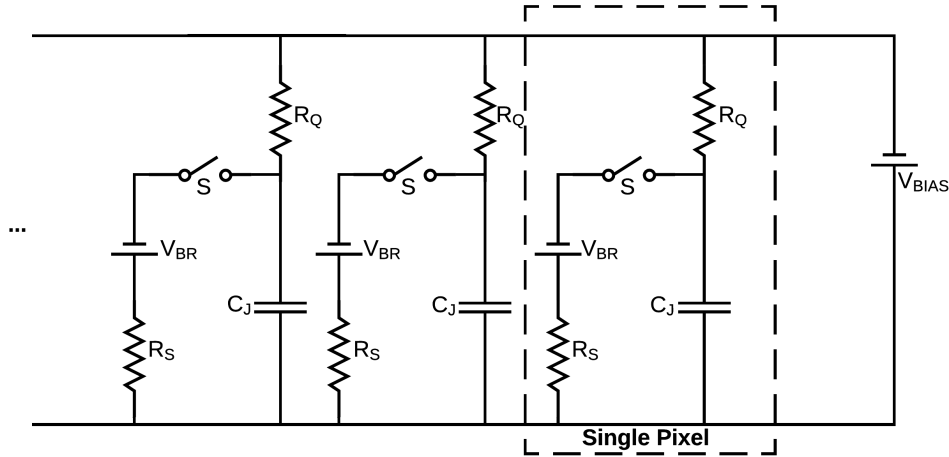


Figure 2.6: Equivalent circuit of a SiPM. Every pixel correspond to an APD with a quenching resistor R_Q in series. All the pixels are connected in parallel and operated in Geiger mode.

When a pixel recovers from the avalanche, its C_J recharges to the nominal voltage V_{BIAS} . At the outset of the recharge process, the current flows from V_{BIAS} but also from the junction capacitors of all other pixels. The latter current keeps lowering ΔV on the other pixels until the value is equal to the ΔV on the recovering pixel. At this instant, V_{BIAS} becomes the only current, and all of the pixels recharge together to V_{BIAS} .

2.3 Performance parameters of a SiPM

Important parameters of a SiPM are: the gain M , the breakdown voltage V_{BR} , the quenching resistance R_Q , the junction capacitance C_J , and the noise components such as the dark count rate (DCR), the optical cross-talk probability (CT) and the after-pulse probability (AP). The following sections define these parameters, as well as introduce experimental techniques to quantify them.

2.3.1 Experimental evaluation of operational parameters

Quenching resistor R_Q The forward-bias current-voltage (I-V) characteristics of a SiPM (see figure 2.7 left) can be used to measure the value of R_Q . The I-V characteristic can be obtained with a setup shown on the right side of figure 2.7. Assuming that R_Q is the same for each pixel and that $R_Q \gg R_S$, the slope of the linear dependence in the forward-bias region equals to N/R_Q , where N is the number of pixels. So R_Q can be measured as

$$R_Q = \frac{N}{slope}. \quad (2.2)$$

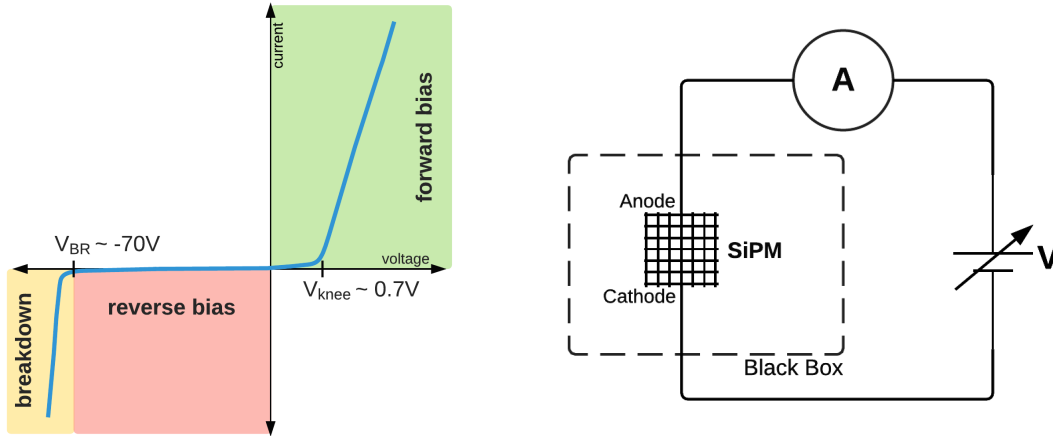


Figure 2.7: (left) Forward and reverse I-V characteristics of a SiPM. (right) The electrical circuit to obtain a forward-bias I-V characteristic, which contains information about R_Q . The SiPM must be shielded from light in a temperature-controlled environment.

Gain M , breakdown voltage V_{BR} and capacitance C_J The gain M is defined as the number of carriers contained in the single-cell current pulse, since this is the number of carriers generated during the avalanche in response to an absorbed photon. Integrating the current pulse shown in figure 2.5 over time yields the total charge Q that is transferred between the terminals of one SiPM pixel. Since the transfer was triggered by a single charge carrier, the gain is equal to

$$M = \frac{Q}{e}. \quad (2.3)$$

A detailed analysis shows that

$$Q = C_J \times \Delta V, \quad (2.4)$$

and thus,

$$M = \frac{C_J \times \Delta V}{e}. \quad (2.5)$$

The setup necessary to measure the gain is shown in figure 2.8 (left). The current pulses generated by the SiPM can be transformed with a read-out circuit into voltage pulses, and read out by a voltage analog-to-digital converter (ADC). The characteristics of possible read-out circuits is described in detail in Chapter 3. The acquired data is stored on a computer for further analysis. A histogram of the measured charge Q of the signal pulses gives a photoelectron (p.e.) charge spectrum of a SiPM (see figure 2.8 middle); it can be used to determine the gain M of the device, using the following equation:

$$M = \frac{U_U \times t_U}{e \times R \times K_{amp}} \times 1\text{p.e.} \quad (2.6)$$

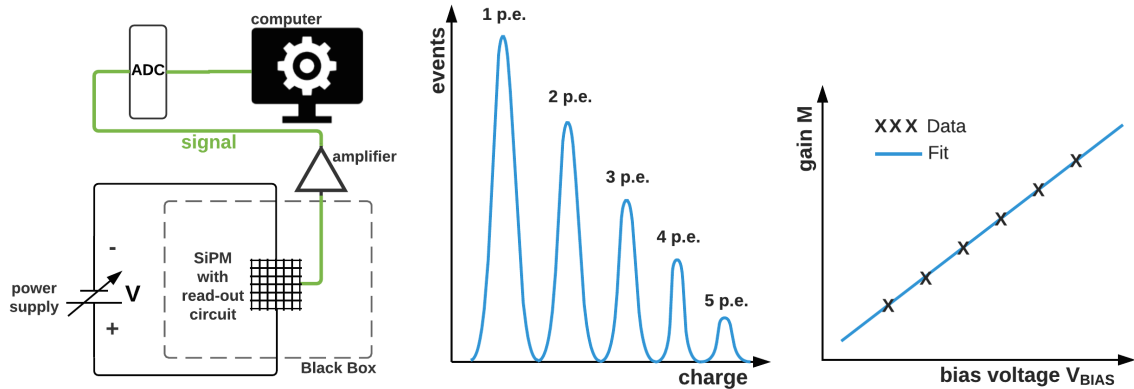


Figure 2.8: (left) Experimental setup to measure the gain and the breakdown voltage. (middle) Sketch of a charge photoelectron (p.e.) spectrum with 5 visible p.e. peaks. The position of the 1 p.e. is used to calculate the gain. (right) Sketch of the gain versus bias voltage of a SiPM. A linear fit can be used to determine the breakdown voltage and the junction capacitance.

where U_U is the voltage per channel of the ADC, t_U is the time of one sample of the ADC, 1p.e. is the position of the single photoelectrons peak in the charge spectrum, K_{amp} is the amplification factor of the electronics, R is the input impedance of the ADC and e is the electron charge. The gain M can be determined as a function of V_{BIAS} by collecting photoelectron spectra for various settings of V_{BIAS} . The expected relationship between M and V_{BIAS} is linear as shown in figure 2.8 (right). Fitting a straight line to the data yields the values of C_J and V_{BR} using the slope and the vertical interception respectively:

$$V_{BR} = V_{BIAS} \quad \text{at} \quad M = 0,$$

$$C_J = slope \times e.$$

(2.7)

2.3.2 Noise components of a SiPM

Noise in SiPMs is represented by output current pulses produced in absence of incident light. A SiPM generates three different noise components: dark noise also called dark counts (DC), optical cross-talk (CT) and after-pulses (AP). Figure 2.9 is a screen shot of an oscilloscope output while acquiring data of a SiPM in a dark environment [36]. The discrete structure of the 1 p.e. 2 p.e. and 3 p.e. becomes visible. The 1 p.e. signals, arising from the primary dark noise, are more abundant than the 2 p.e. and 3 p.e. signals induced by optical cross-talk. The visible signal pulses following the primary signals are detected after-pulse events.

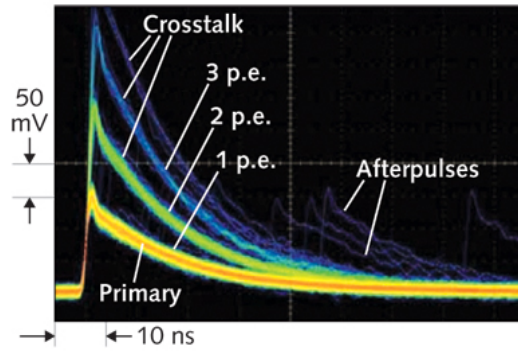


Figure 2.9: Oscilloscope screen shot with visible noise components. Figure adapted from [36].

In the following paragraphs a detailed description of the different noise components is given and their measurement methods are presented.

Dark counts In silicon, there is a finite probability $p(T)$ for charge carriers to be generated by thermal excitation, given by

$$p(T) = CT^{3/2} \exp\left(-\frac{E_g}{2k_B T}\right), \quad (2.8)$$

where T is the absolute temperature, E_g is the bandgap energy, k_B is the Boltzmann constant and C is a proportionality constant depending on the material and the technological parameters. Such a generated electron or hole originates inside the active region of a pixel of the SiPM and can trigger an avalanche, producing an observable output pulse. This primary noise event is called a dark event. The number of dark events per unit time is the dark count rate (DCR). From equation 2.8 one can deduce that, in SiPMs, the thermal generation of carriers doubles approximately every 10°C , and so does the DCR. Moreover, the DCR scales with the SiPM area and is an increasing function of the overvoltage. In a SiPM, dark events have 1 p.e. amplitude and are hence indistinguishable from a photo-generated event. Since the primary noise scales with the silicon area, the DCR can be given as Hz per unit area, with overvoltage and temperature always specified.

The measurement principle of the DCR is explained in the next paragraph.

Optical cross-talk (CT) Optical cross-talk involves photons emitted during avalanche multiplication by recombination of an electron-hole pair. For silicon the wavelength of the produced photons lies within the range of 450 and 500 nm. These photons are re-absorbed in neighbouring cells or even in the inactive region of the same cell and cause additional current pulses.

Direct-CT occurs when an emitted photon reaches the active region of another cell triggering an additional avalanche practically at the same instant of the original one. The result is the double pulse (2 p.e.) in figure 2.9. Delayed-CT involves photons that are re-absorbed in the inactive regions of the SiPM. The generated electron (or hole)

must then diffuse to the active region of a cell before being able to trigger an avalanche. The correlated pulse has therefore a certain time-delay (of the order of few ns) with respect to the original one.

In the absence of light, 2 p.e. (or greater) waveforms originating from a SiPM can be either due to random dark noise occurring in two or more pixels simultaneously or cross-talk. The probability of the former is very small and is therefore neglected. Hence, counting the number of pulses above the 1 p.e. threshold per second yields the cross-talk rate.

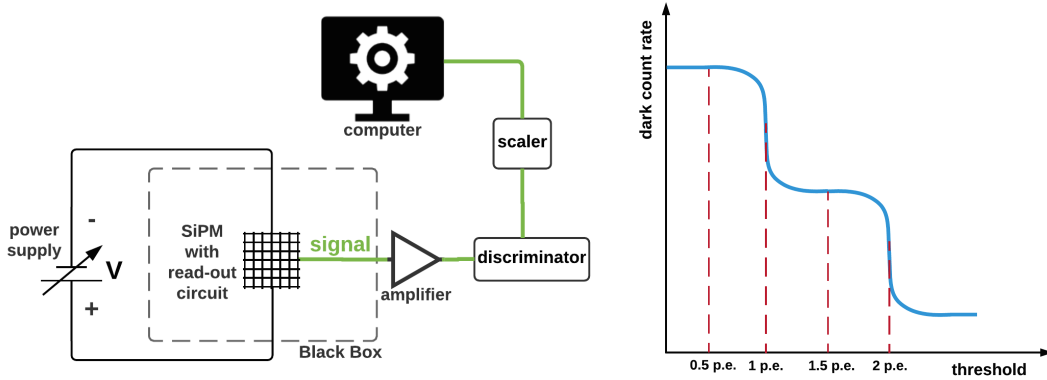


Figure 2.10: (left) Experimental setup to measure the dark count rate (DCR) and the cross-talk rate (CTR). (right) Sketch of the threshold-dependent dark count rate.

Figure 2.10 left shows the experimental setup to measure the rates (and probabilities) of cross-talk and the DC. The SiPM is reverse-biased by a power supply and placed inside a temperature-controlled and light-tight black box. The output signal from the SiPM is amplified and the resulting signal is fed to a discriminator. If the input crosses a user-specified threshold level, the discriminator issues a logical output pulse which the scaler module counts. Figure 2.10 (right) shows a sketch of the resulting dark count rate as a function of the threshold level. The curve shows that the noise rate decreases with the increasing discriminator threshold levels showing a characteristic step-like dependence. The vertical red dashed lines delineate the values of the DC rate for the corresponding thresholds 0.5 p.e., 1 p.e, 1.5 p.e. and 2 p.e. Setting the threshold level to 0.5 p.e., which is above the electronic noise, but below 1 p.e., gives the rate of the total detected dark noise (DCR). Setting the threshold to 1.5 p.e. gives the rate of the events due to cross-talk (CTR). The probability of cross-talk P_C is therefore given by

$$P_C = \frac{\text{DCR}_{1.5\text{p.e.}}}{\text{DCR}_{0.5\text{p.e.}}} = \frac{\text{CTR}}{\text{DCR}}. \quad (2.9)$$

The cross-talk probability P_C depends on the overvoltage ΔV . The experimental setup depicted in Figure 2.10 (left) can be used to determine this dependence. The procedure is to measure P_C as outlined above for different values of ΔV , which is controlled by the power supply.



After-pulses (AP) After-pulsing is due to charge carriers trapped in silicon defects during the avalanche multiplication that are released later or during the recharge phase of the SiPM pixel. The net effect is that a new current pulse is observed on the tail of the original pulse, see figure 2.9. After-pulse probability increases more than linearly with the overvoltage. The amount of charge released in an after-pulse depends on the time delay Δt between the primary and secondary avalanches, or the recovery state of the pixel. A standard method to measure the probability of after-pulses in a SiPM is by replacing the scaler from the setup in figure 2.10 with a Time-to-Digital Converter (TDC), which measures the time difference for consecutive pulses coming from the discriminator. The model used to determine the after-pulse probability using this method is discussed in detail by [37].

However, in the scope of this thesis a different approach has been developed to measure the after-pulse probability by further investigations of the gain calibration data. The analysis approach used to determine the after-pulse probability is presented in Chapter 4.

3 Read-out electronics and tested SiPM prototype

There is great freedom in the choice of SiPMs and their read-out circuits. Since the performance requirements of SiPMs depend mostly on the type of experiment in which they are employed, circuits can be designed to suit the specifications. It is a common practice of research groups to be strongly involved in the R&D process with manufacturers, as this allows them to fabricate dedicated hardware to fit the special needs of the experiments.

For the future xenon-based dark matter search experiment DARWIN, the main requirements for SiPM candidates and the design of a suitable read-out board are the following:

- high gain ($\sim \text{few} \times 10^6$)
- low noise (DC, CT, AP)
- low intrinsic radioactivity
- stable operation in liquid xenon
- high photosensitive area coverage
- optimal sensitive area per channel ratio

To address the second and the last three requirements listed above, three different types of read-out boards have been designed and tested. This chapter presents the investigated SiPM prototype from Hamamatsu in the next paragraph and the different designs of the read-out circuits for this specific SiPM are motivated and presented in the sections 3.1 and 3.2.

Hamamatsu 10943-3186(x) Type A SiPM The Hamamatsu $12 \times 12 \text{mm}^2$ SiPM 10943-3186(x) is an array of 4 separate $6 \times 6 \text{mm}^2$ vacuum ultraviolet sensitive SiPMs merged in one device (see figure 3.1). Each $6 \times 6 \text{mm}^2$ SiPM (segment) has its own 2 pins (cathode and anode). This gives the possibility of reading every segment separately or in various combinations.

Figure 3.1 shows a technical drawing of the tested SiPM. The specifications given by the manufacturer are listed in table 3.1.

parameter	min	typical	max	unit
spectral response range	-	130 - 900	-	nm
peak sensitivity wavelength	-	430	-	nm
pixel pitch	-	50	-	μm
effective photosensitive area	-	5.95 x 5.85	-	mm^2
recommended operating voltage	60	70	80	V
detection efficiency at $\lambda = 178\text{nm}$	20	25	-	%
dark count/segment	-	7.0	21.0	MHz
capacitance/segment	-	1200	-	pF
Gain at $V_{\text{BIAS}} = 70\text{V}$	-	1.25×10^6	-	-

Table 3.1: Specifications of SiPM 10943-3186(x) Type A at $T = 25^\circ\text{C}$, provided by Hamamatsu.

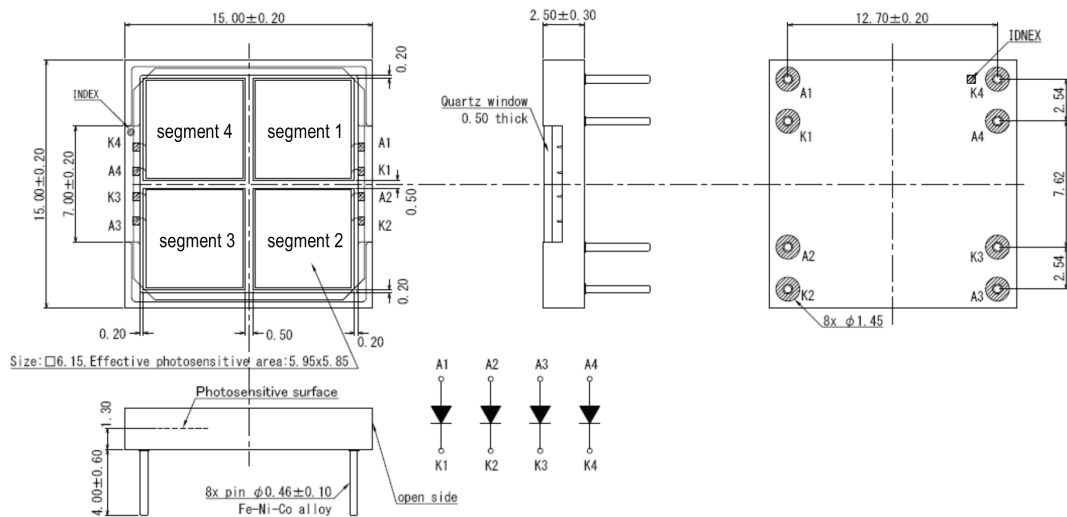


Figure 3.1: Technical drawing of SiPM 10943-3186(x) Type A, provided by Hamamatsu.

3.1 Single-channel read-out electronics

In order to characterize every segment separately, a so called single read-out circuit board was designed. The board contains four exact copies of the schematics shown in figure 3.2 (left) and allows to bias each segment separately. A low-pass filter stabilizes the bias voltage coming from the power supply and cuts off high frequency noise. A SiPM produces small current pulses, as shown in the previous chapter in Section 2.2. In order to measure these pulses with a voltage-ADC, the current signals are fed to a read-out-capacitor, which is equivalent to charging an RC circuit. This process generates measurable voltage signals in the circuit. The arising voltage signals are amplified externally with a commercial low noise amplifier on their way to the voltage-ADC. The prototype PCB-board design is shown in figure 3.2 (right).

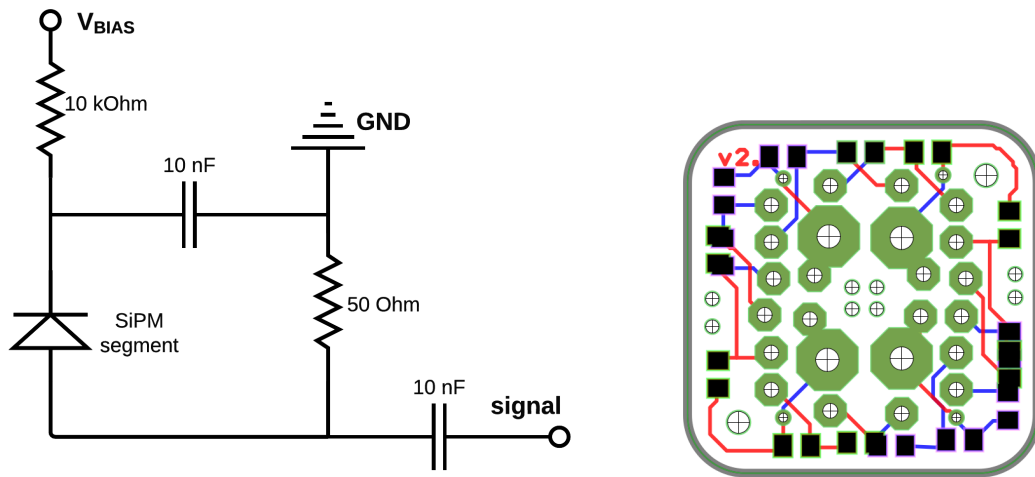


Figure 3.2: (left) Schematic of the single read-out circuit (1 channel). (right) PCB board routing with all four channels. The red and blue lines correspond to the front and back side of the PCB-board respectively.

If the single read-out method would be employed inside a large-volume time-projection chamber, the high number of channels would be a disadvantage: Every channel would need cabling, an amplifier and an ADC input channel. In a dual-phase TPC the, xy-reconstruction of an event is performed by using the information of the light intensity distribution across the top photosensor array. Hence small and abundant photosensors result in a high resolution. A simulation of the XENON1T TPC, using a neural network for the position reconstruction trained with 5×10^3 photons, showed a typical resolution of 4.5 mm in the x-y plane [38]. Considering that the area of the XENON1T PMTs is about 30 times bigger than the area of all the four segments of the given SiPMs, there will be no need to read the segments separately in DARWIN. The required xy-position resolution of a few mm allows it to combine more SiPM segments in one channel, reducing the total number of read-out channels. This gives the motivation to find a suitable method of reading more segments per channel. In order to evaluate the optimal sensitive area per

channel ratio further investigations are necessary. In the following sections the methods of reading all four segments of the SiPM simultaneously are discussed.

3.2 Multi-channel read-out electronics

There are different ways of merging the signals of all segments of a SiPM into one read-out channel. The simplest examples are to put all segments in parallel or in series. The following paragraphs show the consequences of these two choices and introduce a more advantageous method of a combined read-out.

Parallel connection The configuration of all four segments in parallel is equivalent to a single SiPM with a four times larger area. This increases the capacitance of the SiPM by the same factor. As seen in figure 2.5, the time-constant of the pulses is proportional to the junction capacitance C_J , leading to longer signal pulses (see figure 3.3 orange line). The decay time for a single segment is $\sim 50\text{ns}$, while four segments in parallel show $\sim 200\text{ns}$. This can be an issue for high-rate measurements (above 5 MHz) and might worsen the performance of the SiPM.

Serial connection On the other hand, a serial connection of all four segments would reduce the capacitance. Hence it would improve the time characteristics (decay time of $\sim 30\text{ns}$) of the SiPM (see figure 3.3 blue line). A drawback of this configuration is that the bias voltage is shared by all the segments, leading not just to a higher overall voltage but to the fact that the different segments are no longer on the same electrical potential. Possible electric discharges between the segments become an issue.

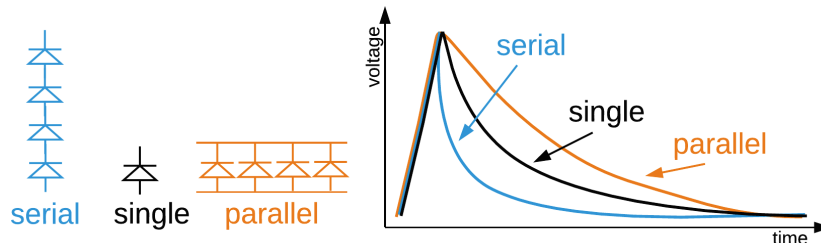


Figure 3.3: Signal pulse shape of a SiPM for serial, single and parallel read-out with respective decay times of $\sim 30\text{ns}$, $\sim 50\text{ns}$ and $\sim 200\text{ns}$.

The so-called hybrid read-out circuit [39] combines the advantages of a serial and a parallel connection of the four segments (see figure 3.4). By powering the segments in parallel, the danger of discharges between the segments disappears. The signals on the other hand are connected in series by decreasing the overall capacitance of the circuit, providing short signal pulses and therefore increasing the performance of the detector.

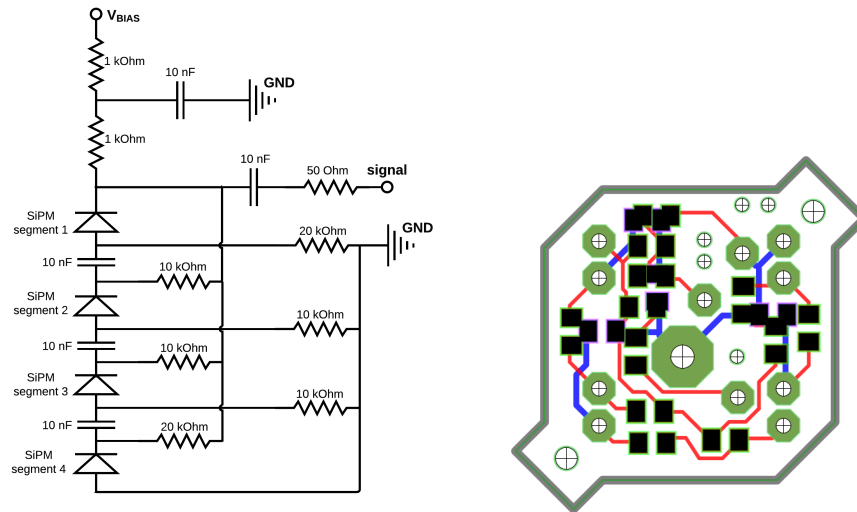


Figure 3.4: (left) Schematic of the hybrid read-out circuit. (right) PCB routing of the hybrid read-out. The red and blue lines correspond to the front and back side of the PCB-board respectively.

Performance test In order to test the hybrid read-out prototype circuit, a gain measurement using the dark count data was performed in a black-box. The signal pulses in the acquired waveforms are shown in figure 3.5 (left). The resulting photoelectron spectrum did not show any peaks, hence the measured pulse areas were exponentially distributed. This makes it impossible to perform a gain calibration. The SiPM manufacturer (Hamamatsu) explained this behaviour as the result of a not stable baseline of the device. This means that after a signal pulse, the previous baseline is not reached fast enough before another pulse occurs. This results in a random integration of the pulses, which results in a charge spectrum without resolved p.e. peaks as shown in figure 3.5 (right). The next-prototype SiPM generation should no longer show this behaviour.

3.3 Pre-amplifier read-out electronics

New generation dark matter search experiments increase the target mass to increase the sensitivity. Since usually the data acquisition system is placed far away from such big detectors, the signal cables can become very long. This will be the case with the DARWIN experiment, as it is already with XENON1T. Long signal cables mean also larger signal damping, distortion and noise pickup. This makes it more important to place the signal amplifier as close as possible to the detector. The ideal place of the amplifier is directly on the read-out circuit, such that the damping of the signal before being amplified is reduced to zero. This was the motivation of developing a pre-amplifier read-out circuit. The prototype presented here is a first version with four output channels amplifying the output voltage of each segment separately. The schematic of one channel

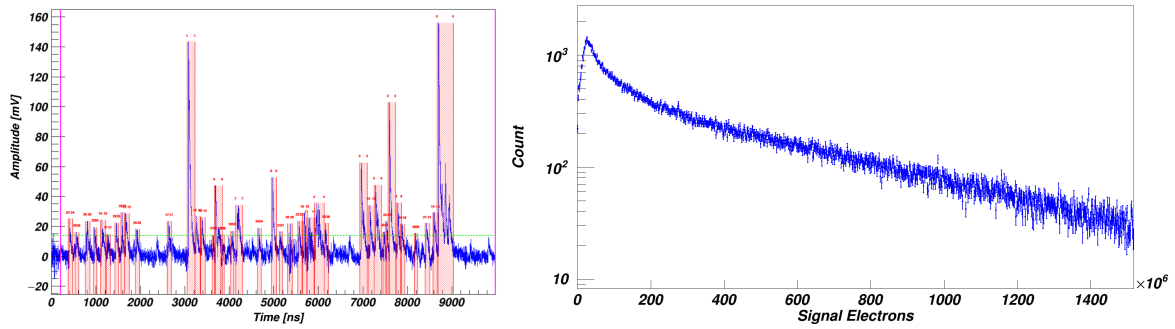


Figure 3.5: (left) Waveform acquired with the hybrid read-out board, containing numerous 1 p.e. events and some higher p.e. cross-talk events. The first 200ns of the waveform are used to calculate the baseline. If a signal exceeds the threshold of 3 times the baseline, the peak is integrated (red shades area) and stored in an output file. (right) Photoelectron spectrum acquired with a hybrid read-out board, without resolved p.e. peaks.

is shown in figure 3.6. The central piece of the circuit is a Texas Instruments low noise operational amplifier OPA847 [40], used as a non-inverting voltage feedback amplifier.

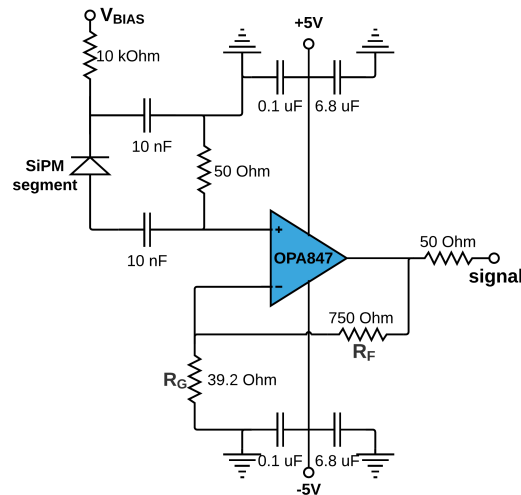


Figure 3.6: Schematic of single read-out pre-amplifier circuit with a gain of 20. The central piece is a non-inverting voltage feedback operation amplifier.

Non-inverting voltage feedback operational amplifier In the amplifier configuration shown in figure 3.7 (left), the input voltage signal (V_{in}) is applied directly to the non-inverting (+) input terminal which means that the output gain of the amplifier becomes “positive”. The result of this is that the output signal is “in-phase” with the input signal.

Since an operational amplifier has very high gain, the potential difference between its inputs tends to zero when a feedback network is implemented. To achieve a reason-

able voltage at the output (and thus equilibrium in the system), the output supplies the inverting input ($-$) (via the feedback network) with enough voltage to reduce the potential difference between the inputs ($+$) and ($-$) to microvolts. In other words V_1 in figure 3.7 is a “virtual earth” summing point. Because of this virtual earth node the resistors R_F and R_G form a simple potential divider network across the non-inverting amplifier.

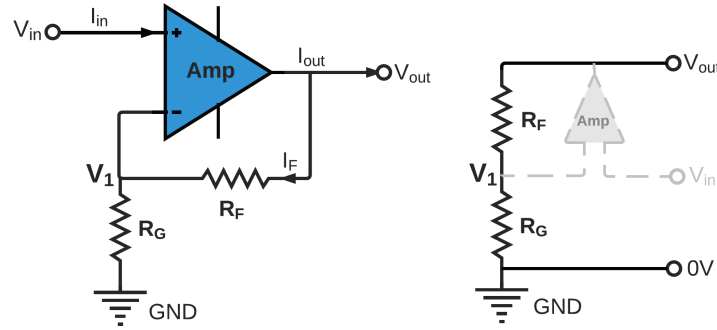


Figure 3.7: (left) Schematic of a non-inverting voltage feedback operational amplifier. (right) Illustration of the corresponding potential divider network across the non-inverting amplifier.

Then using the formula to calculate the output voltage of a potential divider network, the closed-loop voltage gain G of the non-inverting amplifier is determined as follows:

$$V_1 = \frac{R_G}{R_G + R_F} \times V_{out}, \quad (3.1)$$

with $V_1 = V_{in}$ and $G = V_{out}/V_{in}$. The gain G becomes:

$$G = 1 + \frac{R_F}{R_G}, \quad (3.2)$$

where R_F is the feedback resistor and R_G is the ground resistor. The choice of $R_F = 750 \Omega$ and $R_G = 39.2 \Omega$ leads to a gain G of 20.

One can see from equation 3.2, that the overall closed-loop gain of a non-inverting amplifier will always be greater than one (unity) and is determined by the ratio of the values of R_F and R_G .

Performance test At the first stage of the R&D process the pre-amplifier read-out board was tested at room temperature in a dark environment. A sketch of the setup used for this test is shown in figure 3.8 (left).

Using the dark count data, a photoelectron spectrum (see figure 3.8 right) was produced using no additional amplifiers in the electronics. One can clearly identify the various photoelectron peaks. This makes it possible to perform a gain calibration, representing the success of the implementation of this prototype. Future low temperature tests of this amplifier have to be performed, which exceeded the scope of this thesis.

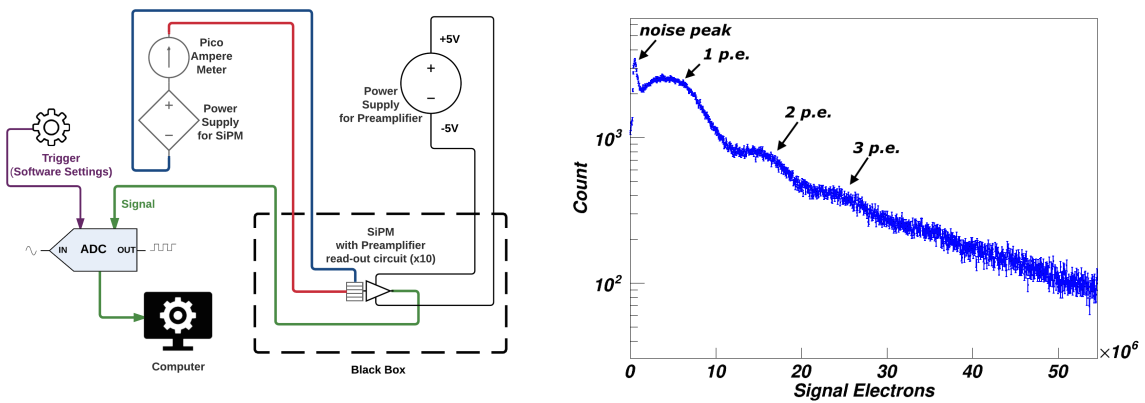


Figure 3.8: (left) Pre-amplifier performance test setup at room temperature. The SiPM and the pre-amplifier were placed inside a black box and biased by external power-supplies. The DC data was amplified only by the pre-amplifier and directly fed to the ADC. (right) Photoelectron spectrum of the SiPM with visible noise peak and p.e. peaks.

4 Measurements and Results

This chapter introduces the experimental set-ups and analytical methods used to measure the performance parameters introduced in Chapter 3 of the Hamamatsu 10943-3186(x) SiPM prototype and summarizes the obtained results. These parameters were measured in a light tight temperature-controlled cryostat, that can be operated in vacuum or gaseous and liquid xenon.

4.1 Forward-bias I-V characteristics

The forward-bias current-voltage (I-V) characteristics have been measured using a voltage controlled Array 3646A power supply with a resolution of 10 mV and a Picotest M3510A pico-ampere-meter with a resolution of 10 nA. The measurement was performed in gaseous xenon (GXe) at room temperature (23.5°C) and in liquid xenon (LXe) at -99.5°C . As expected, the curve behaves linearly for forward voltages above ~ 0.7 V (see figure 4.1). Since the SiPM is designed to have the same values of R_Q for every pixel and the same number of pixels, all segments show exactly the same slope. From the slope of the two curves the values of the quenching resistor R_Q at both temperatures were determined. Considering [11.8 - 14] thousand pixels per segment one gets $R_Q^{\text{warm}} = [13.1, 15.7]\text{M}\Omega$ and $R_Q^{\text{cold}} = [14.7, 17.5]\text{M}\Omega$. This corresponds to a significant increase of the resistance of about 10 % within a temperature interval of 123°C .

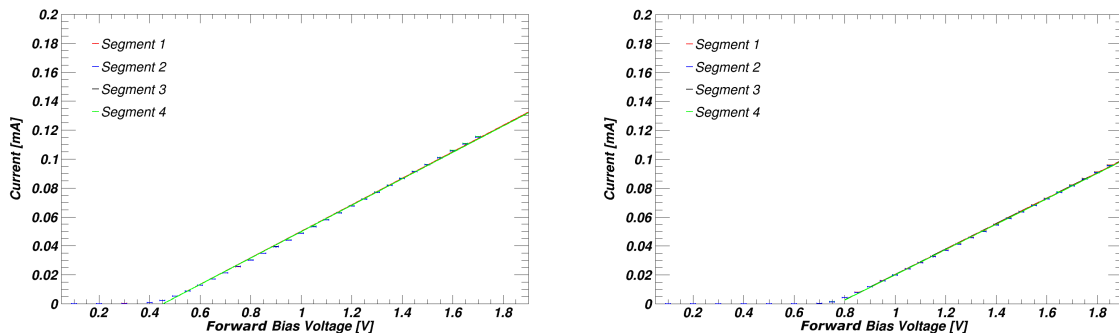


Figure 4.1: (left) Forward-bias voltage I-V characteristics of all segments at 23.5°C temperature, leading to a value of $R_Q^{\text{warm}} = [13.1, 15.7]\text{M}\Omega$. (right) The same at -99.5°C temperature, leading to a value of $R_Q^{\text{cold}} = [14.7, 17.5]\text{M}\Omega$.

4.2 Gain calibration

The experimental set-up (see figure 4.2) used to measure the gain M of the SiPM segments as a function of the overvoltage ΔV consists of a custom-made cryostat that can be operated filled with gaseous or liquid xenon. The insulating vacuum is produced by a turbo-pump and it is set below 10^{-5} mbar. The SiPM is fixed on a PTFE (Teflon) holding structure inside the cryostat (see picture 4.2 right). The external Array 3646A power supply is connected via five SHV feedthroughs (four bias, one ground) to the SiPM read-out board and can be adjusted in 0.01 V steps. The signals pass the cryostat via four BNC feedthroughs and are amplified each by a 100 times commercial low noise amplifier (Rf Bay LNA-1440) before going into the CAEN V1730 flash ADC. The ADC is triggered by a Telemeter TG4001 pulse generator, that is used to operate a blue LED ($\lambda = 470$ nm) inside the cryostat with a frequency of 2.5 kHz. The LED is used for the gain calibration in liquid xenon, since the DCR is too low to be used for the cold measurement. For each set bias voltage (0.1 V steps) the ADC acquires 10^6 trigger events and stores the raw data on a computer.

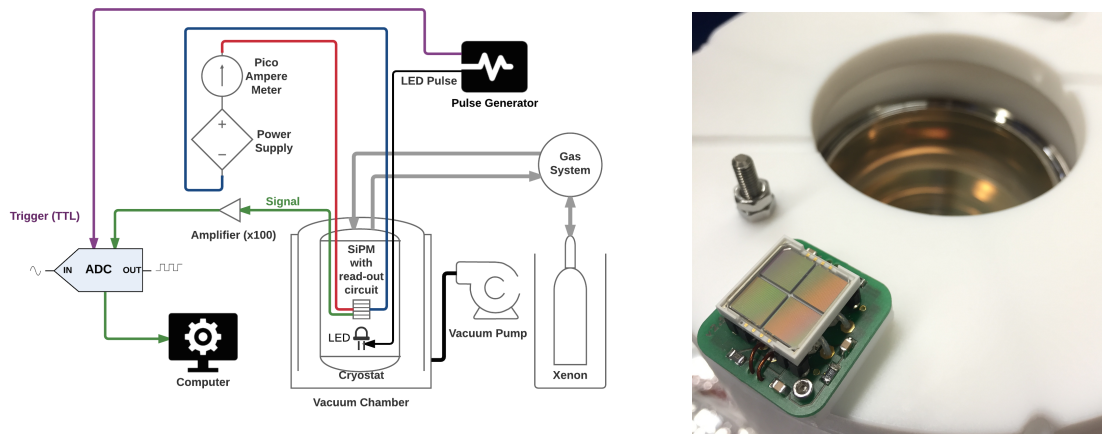


Figure 4.2: (left) Experimental setup for the gain measurements. The temperature-controlled custom-made cryostat can be filled with gaseous or liquid xenon. The SiPM segments are separately biased by a power supply. A pulse generator triggers the ADC and drives an LED for the measurement in LXe. The four signals are amplified and fed to a computer-controlled ADC. The operation of only one segment is shown, although all segments were operated simultaneously. (right) Picture of the SiPM on a single read-out board fixed on a PTFE (Teflon) holding structure.

Data processing The acquired data consist of so-called waveforms, containing all the measured signal pulses produced by the SiPM and the electronic noise events. In figure 4.3 (left), one can see an example of such a waveform containing a 1 p.e. event. The first 200 ns are used to calculate the baseline. If there is a pulse inside this interval (on the left of the purple vertical line) the whole waveform is discarded in the later analysis by an applied cut. Once the baseline is known, the peak processor program searches the

waveform for excursions above 3 times the RMS of the baseline (green horizontal dashed line). If this threshold is exceeded, the processor starts to integrate the pulse. As soon as the same threshold is undercut, the integration ends (see the red shaded area). All integrated peaks are then stored in an ROOT [41] output file, where not just the area, but also the peak position, the peak height and the peak width are stored. The histogram of the peak areas (charge of the pulses) shows populations of discrete peak areas with their abundance with respect to other areas. Figure 4.3 (right) shows such a histogram, called photoelectron (p.e.) spectrum. One can clearly identify the electronic noise peak at the very left (symmetric around zero) and the following photoelectron peaks. This spectrum is used to determine the gain M of the corresponding SiPM segment at a given overvoltage.

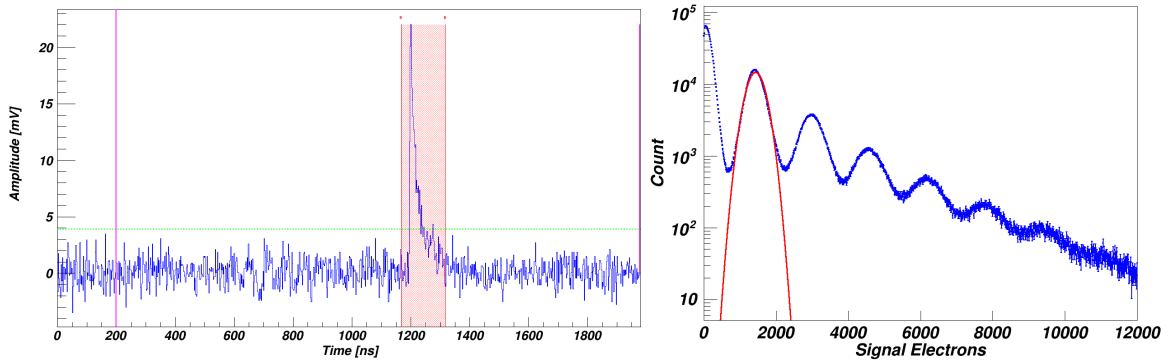


Figure 4.3: (left) Example of a waveform with one single (p.e.) event. The region to the left of the purple line is used to calculate the baseline. The horizontal green dashed line corresponds to 3 times the RMS of the baseline. The red shaded area contains the single peak and marks the integration time window. (right) Example of a photoelectron spectrum with the dominant noise peak around zero and the following p.e. peaks. The red curve is the Gaussian fit for the 1 p.e. peak used for the gain calibration.

Gain calibration results The gain value is determined by fitting the 1 p.e. peak with a Gaussian using ROOT [41] as shown in figure 4.3 (right). The function is equal to

$$f(x) = A \times \exp\left(-\frac{(x - M)^2}{2\sigma_M^2}\right), \quad (4.1)$$

where A is the peak height, M the peak position (gain) and σ_M the standard deviation of the Gaussian. Figure 4.4 shows the behaviour of the gain of all segments as a function of their overvoltage ΔV at room temperature 23.5°C in GXe and in LXe at -99.5°C.

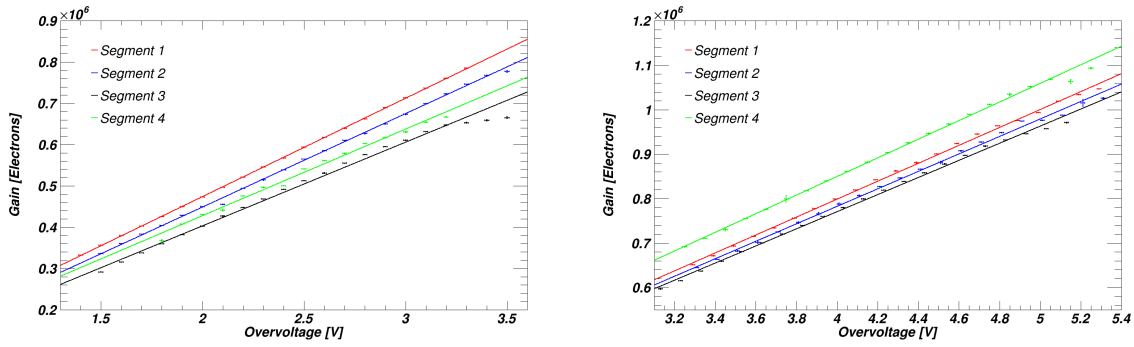


Figure 4.4: (left) Gain calibration curve in GXe at 23.5°C with overvoltages from 1.4-3.5 V. (right) Gain calibration curve in LXe at -99.5°C with overvoltages from 3.1-5.3 V.

Segment	$V_{BR}^{23.5^{\circ}C}$ [V]	$V_{BR}^{-99.5^{\circ}C}$ [V]
1	-64.0	-56.4
2	-64.2	-56.2
3	-63.8	-56.3
4	-64.0	-56.2

Table 4.1: The breakdown voltages V_{BR} for each segment in LXe and GXe. Note the ~ 8 V drop from warm to cold and the remarkable agreement between different segments (error ± 0.1 V).

As expected the gain grows linearly with the overvoltage. The data has been fitted using the linear function

$$g(x) = p_0 + p_1 \times x, \quad (4.2)$$

where p_0 is the y-axis intercept and p_1 the slope of the function. The different segments show slightly different gains, but the same behaviour. The breakdown voltages ($V_{BR} = \frac{p_0}{p_1}$) corresponding to the plots in figure 4.4 are shown in table 4.1. At liquid xenon temperature, higher overvoltages can be reached and thus higher gains. This is because the much lower DCR is keeping the baseline more stable. The peak resolution of one fitted p.e. Gaussian is given by;

$$Res = \frac{\sigma_M}{M} \times 100[\%], \quad (4.3)$$

and is therefore an indicator of the peak width normalized by the gain. Figure 4.5 shows the peak resolution as a function of the overvoltage. There is clearly a maximum at around 2.1 V for the measurements at 23.5°C and at around 4.5 V for the measurement at -99.5°C. The resolution quickly worsens after reaching the optimum (especially in the warm measurement) due to the unstable baseline that makes impossible to integrate the measured waveforms properly. Note that the resolution in cold is better by a factor of ~ 3 respect to warm. This is because an LED was used for the gain calibration in cold due to a very low DCR. The employed blue LED produces a photon spectrum with

a narrow wavelength peak around $\lambda = 470\text{nm}$, which enhances the corresponding peak resolution of the gain measurement.

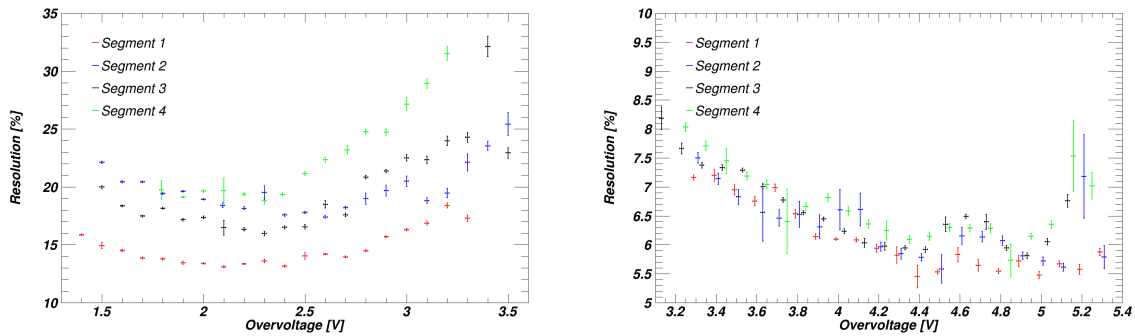


Figure 4.5: (left) The 1 p.e. peak resolution as a function of the overvoltage at 23.5°C , with an optimum at about 2.1 V. (right) The 1 p.e. peak resolution as a function of the overvoltage at -99.5°C , with an optimum at about 4.5 V.

4.3 Dark count rate

Experimental set-up In order to measure the DCR as a function of the overvoltage, the same custom-made cryostat shown in Section 4.2 was used. The ADC has been replaced by a CAEN V895B discriminator and a CAEN V830AC scaler module connected to a computer (see figure 4.6). The discriminator produces an output signal if the input exceeds an adjustable threshold. The scaler module counts the events per units of time and stores the event rates in a ROOT file on the computer.

Data acquisition and analysis By sweeping through different thresholds of the discriminator and acquiring the data with the scaler module during a fixed time-window, the threshold-dependent DCR can be measured (see figure 4.7 left). Since one expects discrete pulse areas (see figure 4.3 right), one expects also discrete pulse heights. These p.e. populations in height manifest themselves in DCR plateaus. Once the threshold of one p.e. population is exceeded the rate drops drastically to a lower plateau. By acquiring datasets for different overvoltages one can see the resulting curve evolution, represented in figure 4.7 (left) with different colors.

As mentioned in Chapter 2, the DCR is defined as the dark count rate at 0.5 p.e., threshold. In order to know exactly the value of 0.5 p.e. the gain calibration data were used to fit the peak height at each overvoltage (see figure 4.7 right). The fit technique is the same as used for the gain calibration using equation 4.2 as a fit function. Knowing the threshold value of 0.5 p.e. one can extract the overvoltage-dependent DCR from the spectra shown in figure 4.7 (left). Since the used discriminator has a threshold resolution of only 1 mV and the calculated 0.5 p.e. threshold resolution is 0.1 mV, the used values are given by the TGraph Eval ROOT [41] function that interpolates in between the two most proximate real measured DC rates.

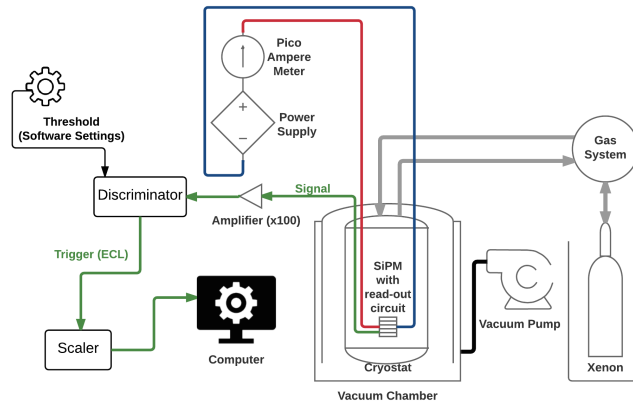


Figure 4.6: Experimental setup for the DCR measurements as a function of the overvoltage and threshold. The temperature-controlled custom-made cryostat can be filled either with gaseous or liquid xenon. The SiPM segments are separately biased by a power supply. The signals are amplified and fed to a computer-controlled discriminator module. The scaler module measures the DC rates for given overvoltages and thresholds. The operation of only one segment is shown, although all segments were operated simultaneously.

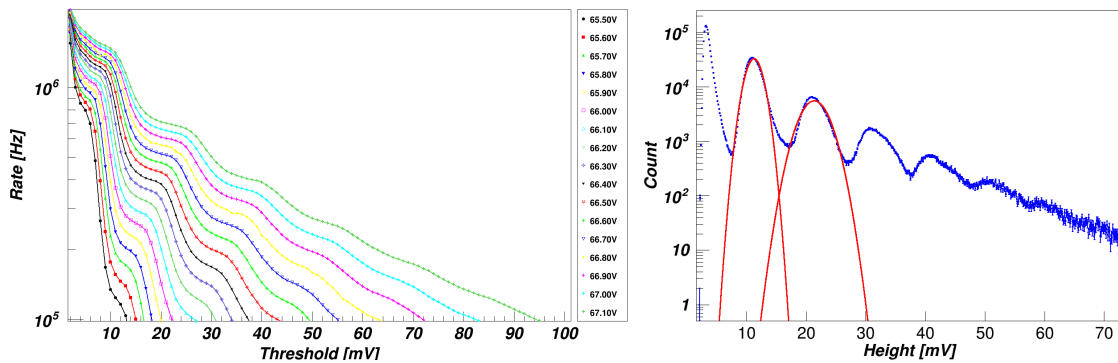


Figure 4.7: (left) Measurement of the threshold-dependent DCR of segment 1 in warm. The coloured curves represent different bias voltage settings. (right) Pulse amplitude p.e. spectrum. The first two p.e. peaks are fitted by a Gaussian to determine the 0.5 p.e. and the 1.5 p.e. thresholds respectively.

DCR results The expected DCR overvoltage dependency is exponential, but the measured segments of the SiPM show an almost linear behaviour (see figure 4.8). Note the ~ 5 orders of magnitude drop of the DC rate between the measurement at 23.5°C and at -99.5°C temperature. This is the reason for the much larger error bars in the cold data. The rate is too small to reach a comparable statistic within a reasonable time.

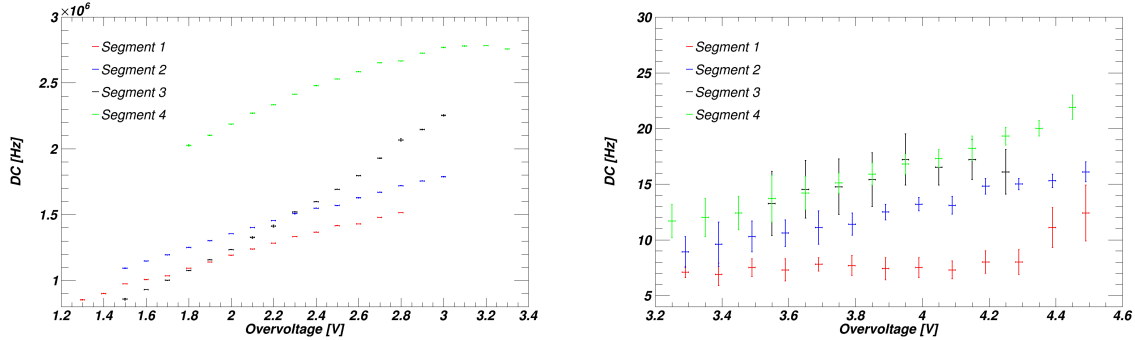


Figure 4.8: (left) Overvoltage-dependent DC rate at room temperature (23.5°C). (right) Overvoltage-dependent DC rate at LXe temperature (-99.5°C). Note the ~ 5 orders of magnitude drop of the DCR from warm to cold.

The average dark count rate per unit area of the tested SiPM prototype is ~ 50 kHz/mm² at room temperature (23.5°C) and ~ 0.3 Hz/mm² at liquid xenon temperature (-99.5°C).

4.4 Cross-talk probability

Data analysis and results In order to evaluate the cross-talk probability the same data from the DCR measurement can be used. The cross-talk probability P_C is defined as the DC rate at 1.5 p.e. over the DC rate at 0.5 p.e. threshold as shown in equation 2.9. By fitting the 2 p.e. peak in the pulse-height spectrum in figure 4.7 (right), one can evaluate the exact threshold for the 1.5 p.e. plateau, analogous to the 0.5 p.e. threshold from Section 4.3.

The cross-talk probability increases linearly with the overvoltage as shown in figure 4.9. As expected there is no temperature dependency, since the overvoltage overlap of the warm and cold measurement show comparable values of P_C . As a general statement one can say that the cross-talk probability of about 50 % is rather high, since other tested SiPM models with a 3×3 mm² active area show values of few % or less [42].

4.5 After-pulse probability

As mentioned in Chapter 2, a new developed approach was used in this thesis to evaluate the after-pulse probability (AP). There was no need for additional data acquisition, since the AP probability was extracted from the gain calibration data.

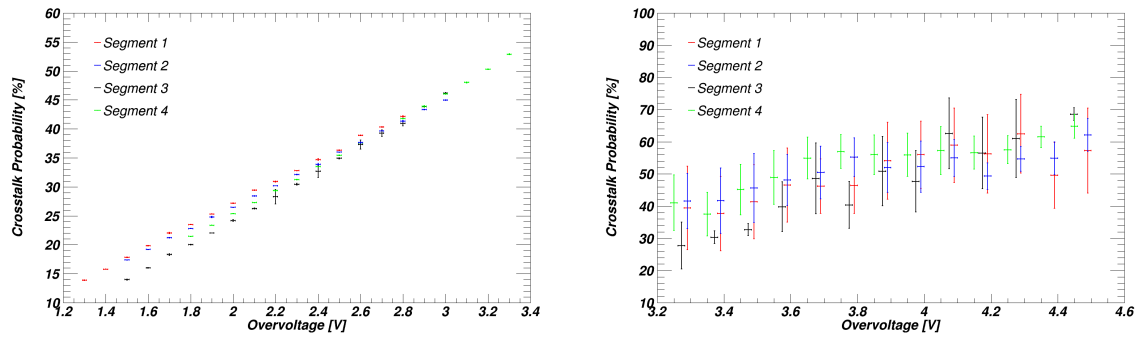


Figure 4.9: (left) Overvoltage-dependent CT probability at room temperature (23.5°C). (right) Overvoltage-dependent CT probability at LXe temperature (-99.5°C). Note the linear dependency and the consistent values in the overlapping interval between 3.2 V and 3.4 V.

Most after-pulses in SiPM occur very fast after the primary pulse (few ns), making them hard to detect by the peak finder software introduced in Section 4.2. Since these two peaks are so close together, the integration threshold is not undercut and the peak finder integrates them as if they are one single peak. Figure 4.10 shows an example of a primary peak with an after-pulse event integrated as one single event. The standard technique explained in Chapter 2 using a Time-to-Digital Converter (TDC) can easily separate this two events. However, there is a way of exploiting the data acquired from the gain calibration to evaluate the AP probability.

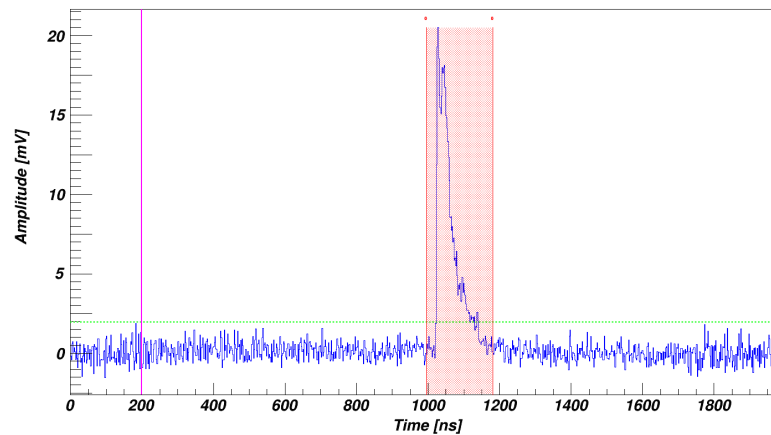


Figure 4.10: A waveform with an after-pulse event. Note the after-pulse peak occurs a few ns after the primary peak. Since the integration threshold (dashed line) is not undercut in-between the two peaks, the peak-finder algorithm integrates them as one event. This integrated peak, has the same height as a normal 1 p.e. event but a larger area, since more charge was released.

After-pulse analysis A pulse as shown in figure 4.10 has a similar amplitude (height) of a normal 1 p.e. event, but since an after-pulse was integrated within this pulse, the charge (area) is larger. The later the after-pulse occurs, the larger is the area of the integrated pulse (reaching a maximum at the 2 p.e. area). As soon as the after-pulse is "late" enough, the peak-finder identifies it as a 1 p.e. event. Thus, the key lies in illustrating the acquired data in a pulse-area (charge) versus pulse-height plot like in figure 4.11. The dominant two-dimensional Gaussian distributed events are the normally integrated 1 p.e. events. The events with similar height but a larger charge are the after-pulse events. By defining an elliptical cut, one can evaluate the ratio between single events and after-pulse events, leading to the after-pulse probability.

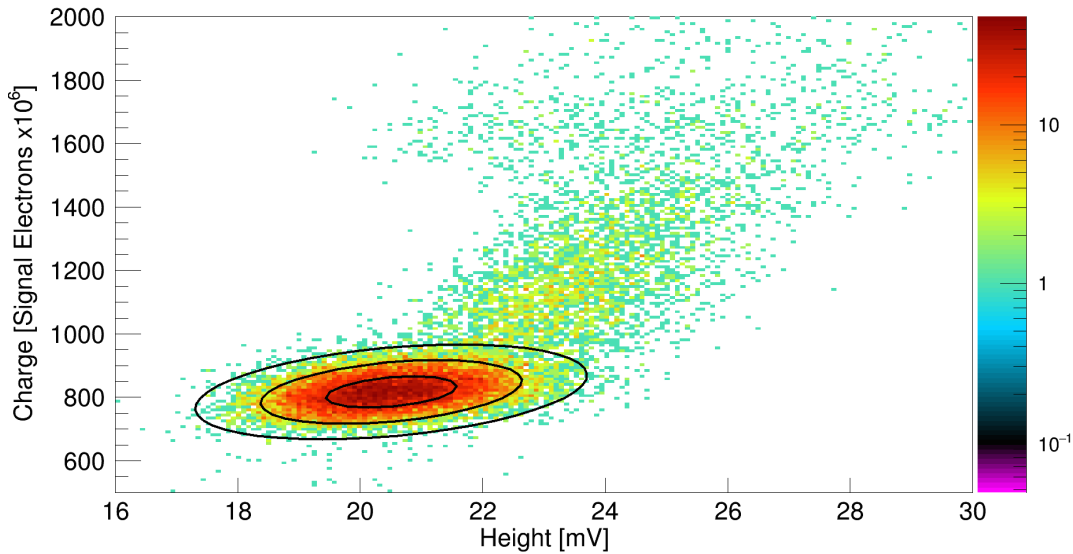


Figure 4.11: (top) Pulse-charge versus Pulse-height representation of the 1 p.e. peak of segment 1 at -99.5°C . The plot range was chosen such that only the 1.p.e. events including the after-pulse events were considered. The three black ellipses on the distribution are the 1 sigma (inner), 2 sigma (middle) and the 3 sigma (outer) line of the 2D-Gaussian fit.

The two-dimensional Gaussian used to fit the dominant 1 p.e. distribution is defined as:

$$f(x, y) = A \times \exp \left[- \left(a(x - x_0)^2 + 2b(x - x_0)(y - y_0) + c(y - y_0)^2 \right) \right],$$

with

$$a = \frac{\cos^2 \theta}{2\sigma_x^2} + \frac{\sin^2 \theta}{2\sigma_y^2};$$

$$b = -\frac{\sin 2\theta}{4\sigma_x^2} + \frac{\sin 2\theta}{4\sigma_y^2} \text{ and};$$

$$c = \frac{\sin^2 \theta}{2\sigma_x^2} + \frac{\cos^2 \theta}{2\sigma_y^2},$$

(4.4)

where A is the amplitude and x_0 and y_0 are the pulse height and integrated charge at the center of the ellipse respectively. σ_x and σ_y are the width parameters in x and y direction and θ is the angle with which the ellipse is rotated in the xy-plane.

The elliptical cut function is then defined as follows:

$$\frac{(x \cdot \cos \theta - y \cdot \sin \theta)^2}{a^2} + \frac{(x \cdot \sin \theta + y \cdot \cos \theta)^2}{b^2} < 1, \quad (4.5)$$

where the major axis a , the minor axis b and the angle θ are defined by the 3 sigma contour of the fit function 4.5. The events inside this ellipse are the primary 1 p.e. events, and all the events outside the ellipse in figure 4.11 are the after-pulse events. By taking the ratio of the after-pulse events over the primary events, one gets the after-pulse probability

$$P_{AP} = \frac{AP_{ev}}{1p.e._{ev}}. \quad (4.6)$$

AP-probability results Figure 4.12 shows the evaluated after-pulse probability as a function of the overvoltage. The expected exponential behaviour and the temperature invariance is confirmed, validating this analysis technique. Nevertheless this method underestimates the real after-pulse probability, since the 1 p.e. population contains also after-pulses, that are well separated from the primary signal peak. Hence those after-pulse events are not distinguishable from the primary events and therefore reduce the after-pulse probability estimated in equation 4.6.

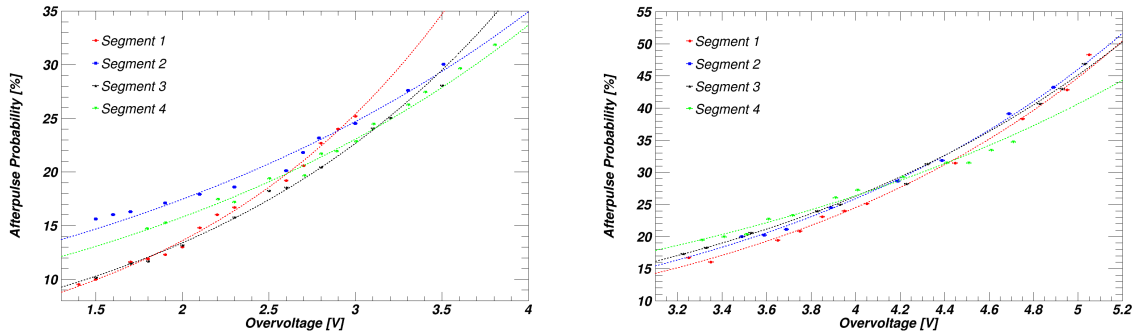


Figure 4.12: (left) The after-pulse probability as a function of the overvoltage at 23.5°C. The dashed lines are fit functions to illustrate the exponential dependency. (right) The after-pulse probability as a function of the overvoltage at -99.5°C. Note the consistent values in the overlapping interval between 3.1 V and 4.0 V, confirming a temperature invariance of the after-pulse probability.

4.6 Scintillation light detection in LXe

In order to confirm the ability of the 10943-3186(x) Type A Hamamatsu SiPM to detect the scintillation light of xenon ($\lambda = 178$ nm), a 30 Bq ^{241}Am source was inserted inside the cryostat. It was attached to the bottom of the cryostat about 2 cm below the SiPM. In figure 4.13 the modified set-up is shown.

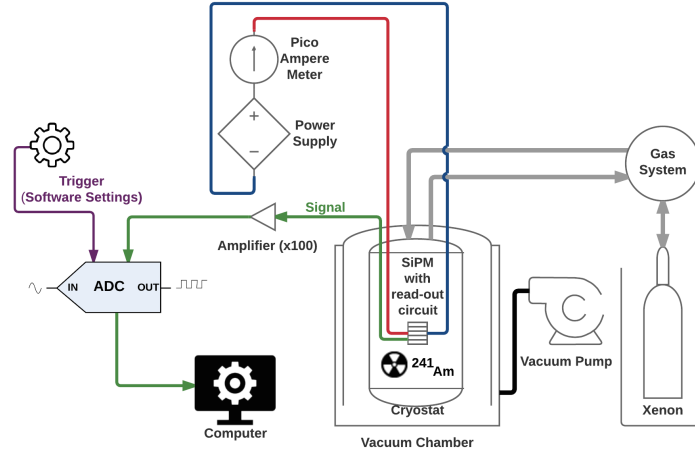
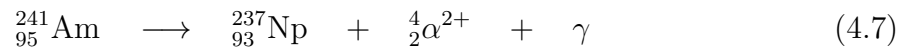


Figure 4.13: Experimental setup for the xenon scintillation light measurement. The 30 Bq ^{241}Am α -particle source is placed inside the cryostat ~ 2 cm below the SiPM while the LXe level was set above the SiPM. The geometry was not optimized for a high light yield, since the main purpose was to measure the presence of scintillation light.

The ^{241}Am source mainly decays via alpha emission combined with a gamma-ray. The α -decay is shown as follows:



About 85% of the generated alpha particles have an energy of 5.486 MeV. The energy spectrum of this source was measured at PSI [43] and is shown in figure 4.14. The γ -ray has an energy of ~ 59.5 keV.

The energetic α -particles may hit the xenon nuclei in the LXe and deposit their energy. Since xenon is a scintillating material, this energy deposition creates photons (see Chapter 1). The wavelength spectrum of the scintillation photons shows a single peak centred at 178 nm, with a width of approximately 10 nm [44].

If the SiPM is sensitive to the wavelength of the scintillation light, an acquired charge spectrum should show a dominant peak at high charge values. Since the energy of the α -particles is known, one can assign an energy to the corresponding peak in the measured spectrum. With this energy calibration, one can determine the light yield of the setup. The light yield is defined as the number of detected photons per deposited energy. This

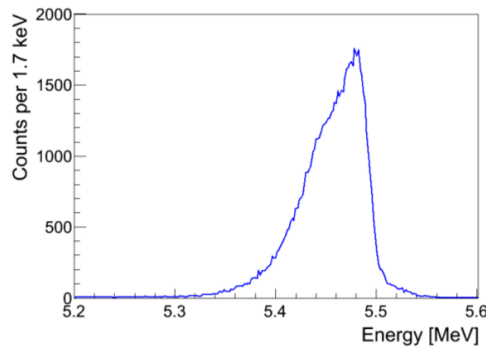


Figure 4.14: Energy spectrum of the employed ^{241}Am α -particle source, measured by [43].

value is wanted to be as high as possible in TPCs and can be optimised by the geometry and the choice of the used materials inside the detector.

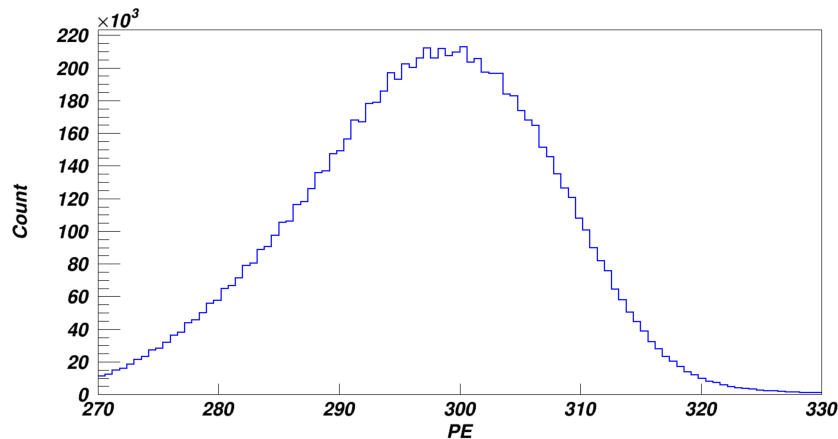


Figure 4.15: Acquired α -particle spectrum of the 10943-3186(x) Type A SiPM. The x-axis is in units of photoelectrons (p.e.) and the α -peak shows a mean value of ~ 299 p.e., corresponding to a light yield of ~ 54.5 p.e./MeV.

In figure 4.15 the acquired charge spectrum is shown. The α -particle population is in the high-energy region and has a mean of ~ 300 photoelectrons. This confirms that the investigated SiPM is able to detect xenon scintillation light. Performing an energy calibration of this spectrum using the α -particle energy from figure 4.14, leads to a light yield of the setup of ~ 54.5 p.e./MeV. Such a low value was expected, since the geometry and the materials of the setup were not optimized for a high light yield. The sole purpose of the setup was to confirm the ability of the investigated SiPM to detect xenon scintillation light.

5 Conclusions and outlook

It is clear that to fully satisfy the requirements on photosensors that are imposed by the ambitious objectives of the future dark matter experiment DARWIN, more R&D is to be performed. In Section 5.1 of this chapter the results on the characterized performance parameters are shortly discussed and compared to state-of-the art PMTs. A brief summary of the performed read-out electronics tests is given in Section 5.2 and suggestions of future R&D proceedings are presented in Section 5.3.

5.1 Performance parameters

The gain of the 10943-3186(x) Type A SiPM model in LXe is $\sim 0.9 \times 10^6$ operated at its best 1 p.e. resolution of $\sim 6\%$ (4.4 V overvoltage). This value is lower than the typical gain of $\sim 5 \times 10^6$ of the XENON1T 3" PMTs (Hamamatsu R11410-21). This is an issue that can be compensated with low noise amplifiers and is therefore no urgent parameter to be improved from the manufacturers side.

The dark count rate (DCR) at a temperature of -99.5°C is on average ~ 12 Hz per segment, corresponding to an DCR per unit area of ~ 0.3 Hz/mm². The accidental coincidence probability of two dark count p.e. triggering a S1 event in DARWIN would be $\sim 3.5 \times 10^6$ events per year. The Hamamatsu R11410-21 PMT has a lower DCR by ~ 2 order of magnitude, lowering the accidental coincidence to ~ 350 events per year. Reaching those low DC rates in future SiPMs is a challenge for the manufacturers. In some cases the research groups are deeply involved in finding new solutions, although mostly the dialogue is hindered by the strict secrecy of the company, needed to be a step ahead of their competitors.

The cross-talk probability (CT) measured to be $\sim 50\%$ for the 10943-3186(x) Type A SiPM, is a poor result. Having a high CT can highly affect the measurement, especially faint light signals. A typical value of the CT probability of other SiPM models from the same manufacturer are in the few % range [42] and need to be improved for future prototypes of the SiPM model tested here.

The After-pulse probability (AP) was measured with a non-standard technique that tend to underestimate the real value. This leads to a lower limit of $\sim 32\%$ of the AP probability at an overvoltage of 4.4 V. This value needs to be lowered as well, since other SiPM models show values of $\sim 10\%$ and lower [42]. The after-pulses of a PMT usually arise from residual gases inside the tube and are an indicator of a vacuum leak. Those

pulses are well separated (few μs). This is in contrast to the SiPM after-pulses, arising extremely fast after the primary pulse (few ns) and therefore not easily identifiable.

5.2 Read-out electronics

The single read-out board is a purely R&D device, developed to characterize the segments of the 10943-3186(x) Type A SiPM separately. It works properly in liquid xenon and produces clean signals. Future SiPM models with the same geometry will be characterised with the procedures and read-out boards presented in this work.

The hybrid read-out is the first step to increase the sensitive area of the SiPM per channel, needed for the future dark matter experiment DARWIN. The read-out board works properly in liquid xenon and produces clean signals. However, the performance test was not successful, since no peaks appeared in the acquired charge spectra. Hamamatsu's statement about this behaviour was a not stable baseline of the SiPM, and that the next prototype will perform properly with the hybrid read-out technique.

The pre-amplifier read-out was a first test at room temperature to include an amplifier on the read-out board. The test measurement was a success, showing a proper photoelectron spectrum. A next step would be to test the device in liquid xenon.

5.3 Future R&D plans

During the working process, several ideas for additional measurements and hardware projects emerged, that exceeded the extent of this thesis. In this section, some ideas to carry on the R&D with SiPMs are presented.

Further tests

- The same measurements as presented in this work can be easily repeated for the next prototype generation, since the hardware and techniques are well established. The characterization of the newest Hamamatsu $12 \times 12 \text{ mm}^2$ SiPM prototype 10943-4372 has already being started.
- The pre-amplifier could be tested in a temperature controlled cryostat to evaluate its temperature working range.
- Photons produced by recombination of electron-hole pairs ($\lambda = 450\text{-}500 \text{ nm}$) can also exit the silicon layer, analogous to the light emission of an ordinary LED. This micro-light-emission of a SiPM could be measured using a well understood PMT facing the SiPM in a dark environment. This measurement could be performed at room temperature in a black box and/or in a cryostat at LXe temperatures.



More advanced read-out electronics

- After the hybrid read-out board is confirmed to work with one SiPM, the next step would be to construct a hybrid board that connects more than four segments together, creating a larger hybrid array. The current hybrid board is already designed to form larger arrays like a puzzle.
- The pre-amplifier should be included in the hybrid board, once it is confirmed to operate in liquid xenon.
- Once the two points above are implemented, one could start to design a small SiPM dual-phase xenon TPC as a proof of principle, using a cryogenic pre-amplified hybrid read-out board. At this stage a 4π sensitive area coverage could already be tested.
- The intrinsic radio-activity of the used materials needs to be very low and well known to estimate the total radioactive background of the experiment. Therefore the electronic components and the SiPMs themselves need to be screened.

Bibliography

- [1] **Particle Data Group**, K. A. Olive et al., *Review of Particle Physics*, *Chin. Phys.* **C38** (2014) 090001.
- [2] G. R. Blumenthal, S. Faber, J. R. Primack and M. J. Rees, *Formation of Galaxies and Large Scale Structure with Cold Dark Matter*, *Nature* **311** (1984) 517–525.
- [3] M. Davis, G. Efstathiou, C. S. Frenk and S. D. White, *The Evolution of Large Scale Structure in a Universe Dominated by Cold Dark Matter*, *Astrophys.J.* **292** (1985) 371–394.
- [4] D. Clowe et al., *A Direct Empirical Proof of the Existence of Dark Matter*, *Astrophys.J.* **648** (2006) L109–L113, [astro-ph/0608407].
- [5] **WMAP** collaboration, C. Bennett et al., *Nine-Year Wilkinson Microwave Anisotropy Probe (WMAP) Observations: Final Maps and Results*, *Astrophys.J.Suppl.* **208** (2013) 20, [arXiv:1212.5225].
- [6] **Planck** collaboration, P. A. R. Ade et al., *Planck 2015 results. XIII. Cosmological parameters*, [arXiv:1502.01589].
- [7] G. Steigman and M. S. Turner, *Cosmological Constraints on the Properties of Weakly Interacting Massive Particles*, *Nucl.Phys.* **B253** (1985) 375.
- [8] G. Jungman, M. Kamionkowski and K. Griest, *Supersymmetric Dark Matter*, *Phys.Rept.* **267** (1996) 195–373, [hep-ph/9506380].
- [9] G. Bertone et al., *Particle Dark Matter - Observations, Models and Searches*. Cambridge University Press, 2013.
- [10] E. Aprile, et al., *Scintillation response of liquid xenon to low energy nuclear recoils*, *Physical Review D* **72**, 072006 (2005).
- [11] **XMASS** collaboration, H. Takiya et al., *A Measurement of the Time Profile of Scintillation Induced by Low Energy Gamma-rays in Liquid Xenon with the XMASS-I Detector*, (2016) [arXiv:1604.01503v1].
- [12] T. Marrodan Undagoitia and L. Rauch, *Dark Matter Direct-detection Experiments*, *J. Phys.* **G43** (2016), no. 1 013001, [arXiv:1509.08767].
- [13] **XENON** collaboration, E. Aprile et al., *Dark Matter Results from 225 Live Days of XENON100 Data*, *Phys.Rev.Lett.* **109** (2012) 181301, [arXiv:1207.5988].

- [14] **XENON** collaboration, E. Aprile et al., *Limits on Spin-dependent WIMP-nucleon Cross Sections from 225 live days of XENON100 data*, *Phys.Rev.Lett.* **111** (2013) 021301, [arXiv:1301.6620].
- [15] **LUX** collaboration, D. Akerib et al., *First results from the LUX dark matter experiment at the Sanford Underground Research Facility*, *Phys.Rev.Lett.* **112** (2014) 091303, [arXiv:1310.8214].
- [16] **XENON** collaboration, E. Aprile et al., *Physics Reach of the XENON1T Dark Matter Experiment*, *Submitted to JCAP* (2015) , [arXiv:1512.07501].
- [17] **LZ** collaboration, D. S. Akerib et al., *LUX-ZEPLIN (LZ) Conceptual Design Report*, [arXiv:1509.02910].
- [18] **DarkSide** collaboration, D. Franco et al., *The Search for Dark Matter with low-radioactivity Argon at LNGS, Letter of Intent*, <https://indico.in2p3.fr/event/12120/contribution/1/material/paper/1.pdf> (2015).
- [19] **DarkSide** collaboration, T. Alexander et al., *DarkSide Search for Dark Matter*, *JINST* **8** (2013) C11021.
- [20] M. Schumann, L. Baudis, L. Buetikofer, A. Kish and M. Selvi, *Dark Matter Sensitivity of Multi-ton Liquid Xenon Detectors*, *JCAP* **1510** (2015) 016, [arXiv:1506.08309].
- [21] **PANDA-X** collaboration, A. Tan et al., *Dark Matter Search Results from the Commissioning Run of PandaX-II*, [arXiv:1602.06563].
- [22] **DarkSide** collaboration, P. Agnes et al., *Low Radioactivity Argon Dark Matter Search Results from the DarkSide-50 Experiment*, [arXiv:1510.00702].
- [23] **LUX** collaboration, D. S. Akerib et al., *Improved WIMP Scattering Limits from the LUX Experiment*, [arXiv:1512.03506].
- [24] **DEAP-3600** collaboration, M. Boulay, *DEAP-3600 Dark Matter Search at SNO-LAB*, *J.Phys.Conf.Ser.* **375** (2012) 012027, [arXiv:1203.0604].
- [25] **DARWIN** consortium, L. Baudis, *DARWIN: Dark Matter WIMP Search with Noble Liquids*, *J. Phys. Conf. Ser.* **375** (2012) 012028, [arXiv:1201.2402].
- [26] **DARWIN** consortium, J. Aalbers et al., *DARWIN: Towards the Ultimate Dark Matter Detector*, (2016) [arXiv:1606.07001v1].
- [27] L. Baudis, S. D'Amato, G. Kessler, A. Kish, J. Wulf, *Measurements of the Position-dependent Photo-detection Sensitivity of the Hamamatsu R11410 and R8520 Photomultiplier Tubes*, (2015) [arXiv:1509.04055v2].

- [28] L. Baudis, A. Behrens, A. Ferella, A. Kish, T. Marrodan Undagoitia et al., *Performance of the Hamamatsu R11410 Photomultiplier Tube in Cryogenic Xenon Environments*, JINST **8** (2013) P04026, [arXiv:1303.0226].
- [29] **XENON** collaboration, E. Aprile et al., Lowering the Radioactivity of the Photomultiplier Tubes for the XENON1T Dark Matter Experiment, Eur. Phys. J. **C75** (2015) 546, [arXiv:1503.07698].
- [30] P. Lightfoot, G. Barker, K. Mavrokoridis, Y. A. Ramachers and N. Spooner, *Characterisation of a Silicon Photomultiplier Device for Applications in Liquid Argon Based Neutrino Physics and Dark Matter Searches*, JINST **3** (2008) P10001, [arXiv:0807.3220].
- [31] I. Ostrovskiy et al., *Characterization of Silicon Photomultipliers for nEXO*, IEEE Trans. Nucl. Sci. (2015) 1825, [arXiv:1502.07837].
- [32] Bahaa E. A. Saleh, Malvin Carl Teich, *Fundamentals of Photonics*. John Wiley Sons, Inc. (1991)
- [33] Julian Beckera, Eckhart Fretwursta, Robert Klannera, *Measurements of Charge Carrier Mobilities and Drift Velocity Saturation in Bulk Silicon of 111 and 100 Crystal Orientation at High Electric Fields*, (2010) [arXiv:1007.4432v2].
- [34] Brian F. Aull et al., *Geiger-Mode Avalanche Photodiodes for Three-Dimensional Imaging* Lincoln Laboratory Journal (2002), volume **13**, number 2.
- [35] Anna Vila, Anna Arbat, Eva Vilella and Angel Dieguez, *Geiger-Mode Avalanche Photodiodes in Standard CMOS Technologies*, Electronics Department University of Barcelona (Spain), [<http://cdn.intechopen.com/pdfs/33517.pdf>]
- [36] Hamamatsu *MPPC Modules Selection Guide* (2014) [http://www.hamamatsu.com/images/hamam/katalogi/mppc_kapd0002e.pdf]
- [37] Patrick Eckert et al., *Characterisation Studies of Silicon Photomultipliers*, (2010) [arXiv:1003.6071v2].
- [38] **Xenon** collaboration, Y. Wei, University of Zurich, *Internal Communication* (2016).
- [39] A. M. Baldini et al., *MEG Upgrade Proposal* (2013) [arXiv:1301.7225v2]
- [40] Texas Instruments, *OPA847, Wideband, Ultra-Low Noise, Voltage-Feedback Operational Amplifier with Shutdown*, (2008) [<http://www.ti.com/lit/ds/symlink/opa847.pdf>].
- [41] ROOT - *An Object Oriented Data Analysis Framework*, Proceedings AIHENP'96 Workshop, Lausanne, Sep. 1996, Nucl. Inst. Meth. in Phys. Res. A **389** (1997) 81-86. See also [<http://root.cern.ch/>].



- [42] Andrea Gmuer, *Design and Simulation of a new Time Projection Chamber with Multiple Photodetector Models*, Master Thesis (2016). [<http://www.physik.uzh.ch/groups/groupbaudis/darkmatter/theses/xenon/master/>].
- [43] **PSI Paul Scherrer Institut**, Villigen Switzerland. [<https://www.psi.ch/>].
- [44] J. Jortner, et al., *J. Chem. Phys.* **42**, 4250 (1965).